Electronic Supplementary Information

Revealing the Effect of Host-Guest Complementarity in Supramolecular Monofunctional Platinum(II) Drugs

Shib Shankar Paul,[a,b] Jan Novotný,[a,b,c,*] Jakub Jakubec,[a,b] Kateřina Petrláková,[d] Pia Jurček,[a] Klára Rašková,[a] Michaela Kuchynka,[b,e] Michal Masařík,[d,f] Petr Kulhánek,[c] and Radek Marek[a,b,c,*]

[a] *CEITEC – Central European Institute of Technology, Masaryk University, Kamenice 5, CZ-62500 Brno, Czechia*

[b] *Department of Chemistry, Faculty of Science, Masaryk University, Kamenice 5, CZ-62500 Brno, Czechia*

[c] *National Center for Biomolecular Research, Faculty of Science, Masaryk University, Kamenice 5, CZ-62500 Brno, Czechia*

[d] *Department of Pathological Physiology, Faculty of Medicine, Masaryk University, Kamenice 5, CZ-62500 Brno, Czechia*

[e] *Department of Chemical Drugs, Faculty of Pharmacy, Masaryk University, Palackého třída 1, CZ-61200 Brno, Czechia*

[f] *Department of Physiology, Faculty of Medicine, Masaryk University, Kamenice 5, CZ-62500 Brno, Czechia*

*** Corresponding Authors**

Emails: jan.novotny@ceitec.muni.cz, radek.marek@ceitec.muni.cz

ADDITIONAL MATERIALS AND METHODS

S1. SYNTHESIS OF LIGANDS

All reagents and solvents were purchased from commercial suppliers and used without further purification. Compounds 4-iodopyridine[1] and 1-(4-bromophenyl)adamantane[2] were synthesized as previously reported. Column chromatography was carried out using silica gel (60 Å, 40–63 μm, Fluorochem, UK) as the stationary phase. ^{1}H and ^{13}C NMR spectra were recorded using Bruker Avance NEO 500 MHz NMR spectrometer. NMR chemical shifts (δ) are reported in parts per million (ppm) using residual solvent signal as a reference for the measured spectra in $CDCl_3$ (^{1}H = 7.26, ^{13}C = 77.16). High-resolution mass spectra (HRMS) were obtained on Agilent 6224 Accurate-Mass Time-of-Flight (TOF) mass spectrometer. Samples were ionised atmospheric pressure chemical ionisation (APCI).

Synthesis and characterization of 4-(1-adamantyl)pyridine (L1):

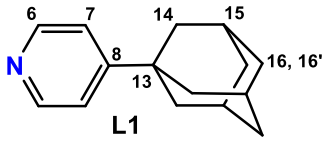

L1

Adapted from a literature procedure.[3] To a solution of 4-iodopyridine (1 g, 4.88 mmol, 1.0 eq.), copper iodide (46 mg, 0.24 mmol, 5 mol-%) and lithium chloride (206 mg, 4.86 mmol, 1.0 eq.) in dry DMF (12 ml) under argon, 1-adamantylzinc bromide solution (0.5 M in THF; 12.7 ml, 1.3 eq.) was added. The yellow solution was stirred at 50 °C for 24 h after which it was cooled to room temperature and diluted with EtOAc and H_2O. Organic layer was washed with sat. Na_4EDTA (aq.) (6x) and sat. Na_2CO_3 (aq.) (3x) to remove the metal salts. The organic layer was dried over anhydrous Na_2SO_4 and evaporated under reduced pressure. The crude was purified by column chromatography (SiO_2, CH_2Cl_2/CH_3OH 39:1). Further purification was done by dissolving the solid in EtOAc and 1M HCl. The mixture was stirred vigorously for 10 min after which the layers were separated. Sat. Na_2CO_3 (aq.) solution was added to HCl layer

until pH ~11 was reached. EtOAc was added to dissolve formed white precipitate. After mixing, EtOAc layer was separated, dried over anhydrous Na_2SO_4, and evaporated under reduced pressure to give L1 (550 mg, 2.6 mmol, 53 %) as an off-white solid. **^{1}H NMR** (500 MHz, 298 K, $CDCl_3$) δ 8.50 (d, J = 6.2 Hz, 2H, H6), 7.23 (d, J = 6.2 Hz, 2H, H7), 2.10 (br, 3H, H15), 1.87 (br, 6H, H_{14}), 1.85 – 1.61 (m, 6H, H16 & H16'). **^{13}C NMR** (126 MHz, 298 K, $CDCl_3$) δ 159.9 (C8), 149.8 (C6), 120.4 (C7), 42.5 (C14), 36.7 (C16 & C16'), 36.3 (C13), 28.7 (C15). **HRMS** (APCI+) *m/z*: $[M+H]^+$ Calcd for $C_{15}H_{19}N$: 214.1590; Found 214.1588.

Synthesis and characterization of 4-(4'-(1-adamantyl)phenyl)pyridine (L2):

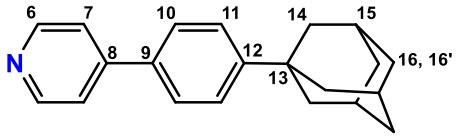

1-(4-Bromophenyl)adamantane (500 mg, 1.72 mmol, 1 eq.), pyridine-4-boronic acid hydrate (253 mg, 2.06 mmol, 1.2 eq.), tetrakis(triphenylphosphine)palladium(0) (60 mg, 0.052 mmol, 3 mol-%), and K_2CO_3 (1.186 g, 8.58 mmol, 5 eq.) were evacuated and backfilled with argon for three cycles. Toluene (10 ml), ethanol (4 ml) and Milli-Q H_2O (3 ml) were sonicated and added to the solids. The yellow solution was heated at 100 °C for 48 h. The mixture was allowed to cool to room temperature and solvents were concentrated under reduced pressure. The crude was dissolved in CH_2Cl_2 and extracted with sat. Na_4EDTA (aq.) (3x) and sat. NaCl (aq.) solution. Organic layer was dried over anhydrous Na_2SO_4 and concentrated under reduced pressure. The crude was purified by column chromatography (Al_2O_3, PE:EtOAc 9:1→3:7). Further purification was done by recrystallization from EtOAc to yield **L2** (260 mg, 0.90 mmol, 52 %) as white solid. **^{1}H NMR** (500 MHz, 298 K, $CDCl_3$) δ 8.64 (d, J = 5.0 Hz, 2H, H6), 7.66 – 7.57 (m, 2H, H10), 7.52 – 7.46 (m, 4H, H7, H11), 2.13 (s, 3H, H15), 1.96 (s, 6H, H14), 1.80 (m, 6H, H16 & H16'). **^{13}C NMR** (126 MHz, 298 K, $CDCl_3$) δ 152.70 (C12), 150.32 (C6), 148.27 (C8), 135.29 (C9), 126.81 (C10), 125.81 (C11), 121.55 (C7), 43.22 (C14), 36.85 (C16

& C16'), 36.38 (C13), 29.01 (C15). **HRMS** (APCI+) *m/z*: $[M+H]^+$ Calcd for $C_{21}H_{23}N$: 290.1930; Found 290.1901.

Synthesis and characterization of 4-pentafluorophenylpyridine (L4):

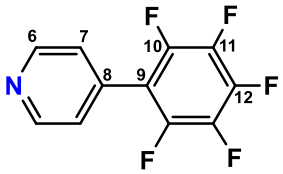

Pyridine-4-boronic acid hydrate (500 mg, 4.07 mmol 1.1 eq.), tetrakis(triphenylphosphine)palladium(0) (128 mg, 0.11 mmol, 3 mol-%) and Na_2CO_3 (2.087 g, 19.69 mmol, 5 eq.) were evacuated and backfilled with argon for two cycles. Degassed dioxane (14 ml), Milli-Q H_2O (3 ml) and iodopentafluorobenzene (493 µl, 3.69 mmol, 1.0 eq.) were added to the reaction mixture which was heated at 95 °C for 48 h. The reaction mixture was cooled down to room temperature and the solvents were removed *in vacuo*. To the remaining residue was added sat. Na_4EDTA (aq.) (20 mL) and DCM (40 ml). The layers were separated, and the organic layer was extracted with sat. Na_4EDTA (aq.) (3x30 ml). The combined organic layer was extracted with sat. NaCl (aq.) (20 ml), dried over anhydrous Na_2SO_4, and concentrated *in vacuo*. The crude was purified by column chromatography (silica, DCM→Et_2O) to yield L4 (178 mg, 0.73 mmol, 20 %) as light orange solid. ^{1}H NMR (700 MHz, 298 K, $CDCl_3$) δ 8.77 (d, J = 5.0 Hz, 2H, H6), 7.37 (d, 2H, H7). ^{13}C NMR (176 MHz, 298 K, $CDCl_3$) δ 150.5 (C6), 144.6 (m, J = 251 Hz, *C*F), 141.4 (m, J = 257 Hz, *C*F), 138.1 (m, J = 253 Hz, *C*F), 134.8 (C8), 124.8 (C7), 113.4 (m, C9). ^{19}F NMR (470 MHz, 298K, $CDCl_3$) δ -142.5 (d, 2F, F10), -160.9 (m, 2F, F11), -152.6 (t, 1F, F12). **HRMS** (APCI+) *m/z*: $[M+H]^+$ Calcd for $C_{11}H_4F_5N$: 245.0264; Found 246.0337.

S2. MASS SPECTROMETRY

Mass spectra of complexes **1**-**4** in methanol (Figure S1a-S1b) and their HG assemblies (Figure S1c-S1e) were studied in aqueous medium in positive ion mode using the electrospray ionization method (ESI-MS). Mass spectra of HG assemblies show three relevant signals, which correspond to free **1**-**4**, HG assembly **1@CB7**-**4@CB7**, and HG aqua-complex **1_aq@CB7**-**4_aq@CB7**.

1 – positive mode, MeOH

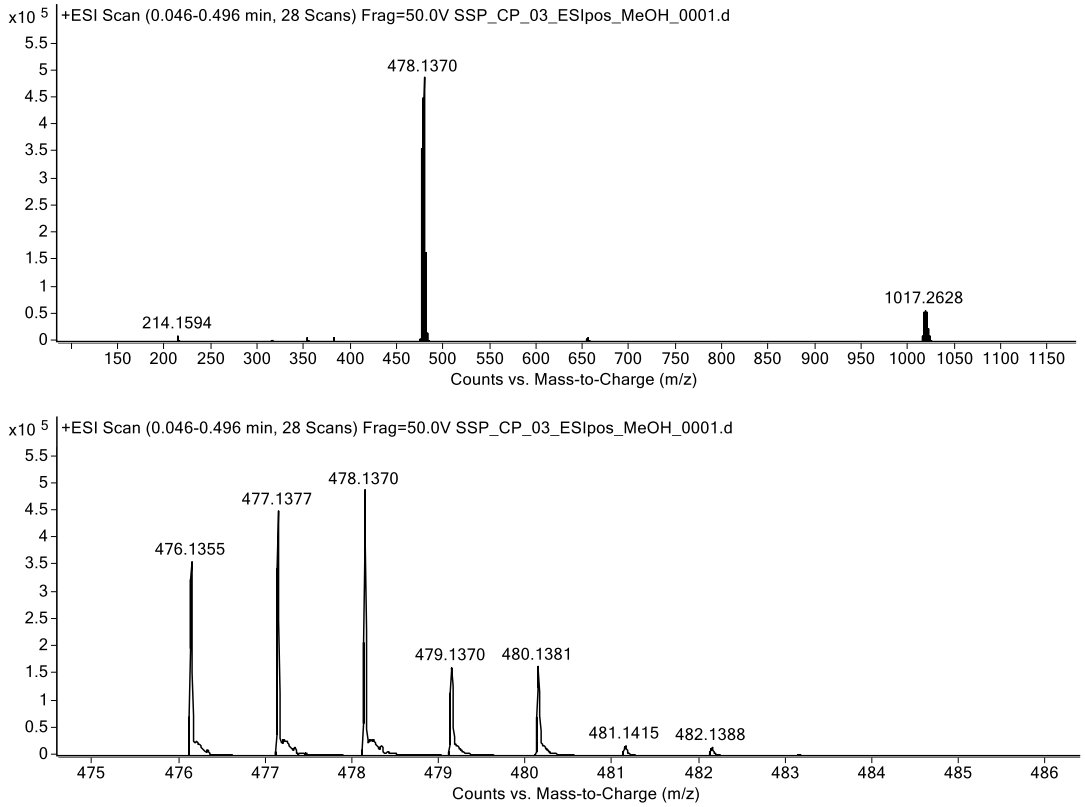

2 – positive mode, MeOH

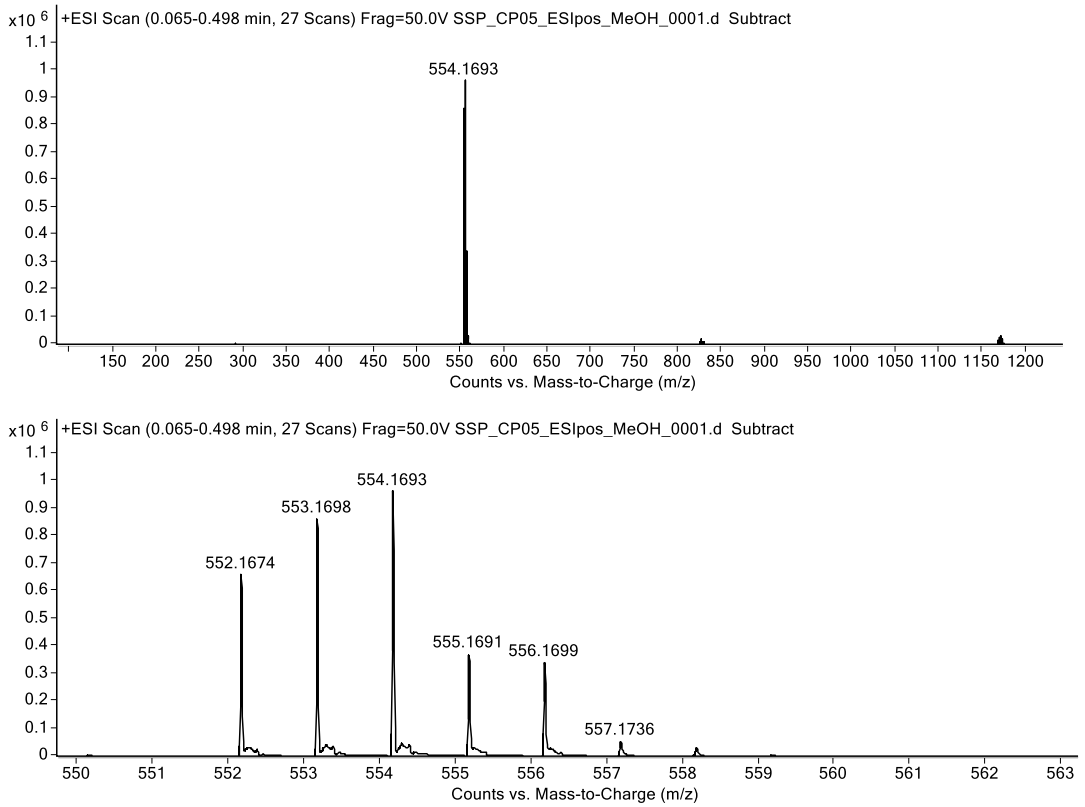

Figure S1a. Results of ESI-MS analyses of compounds **1** and **2**.

3 – positive mode, MeOH

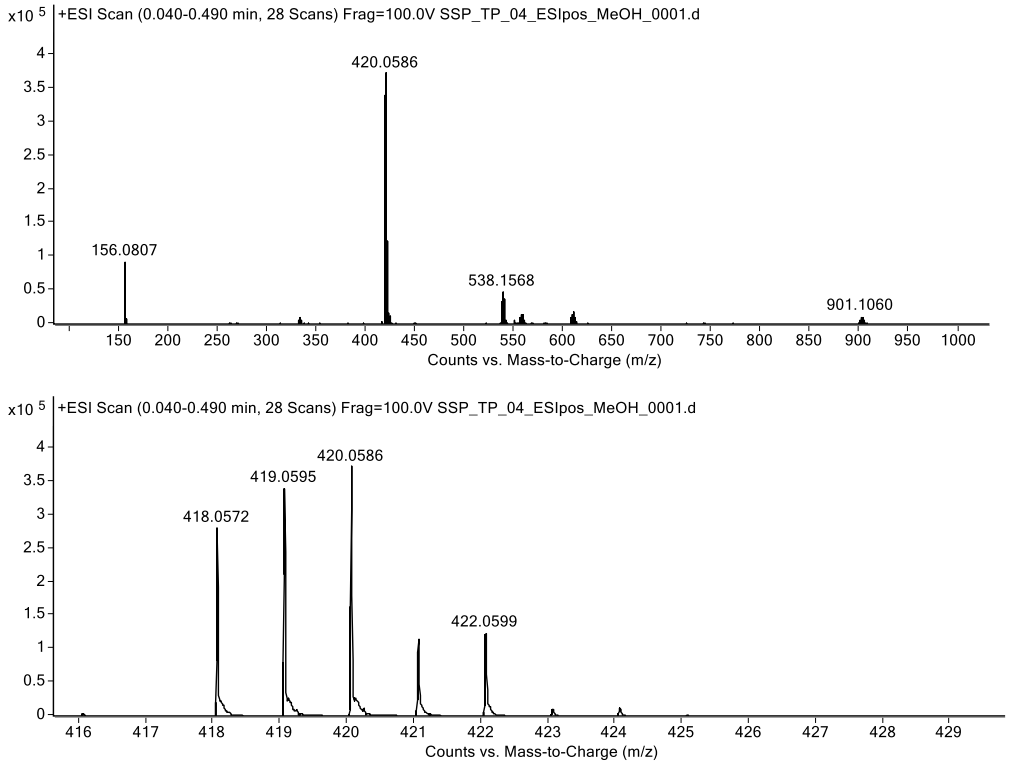

4 – positive mode, MeOH

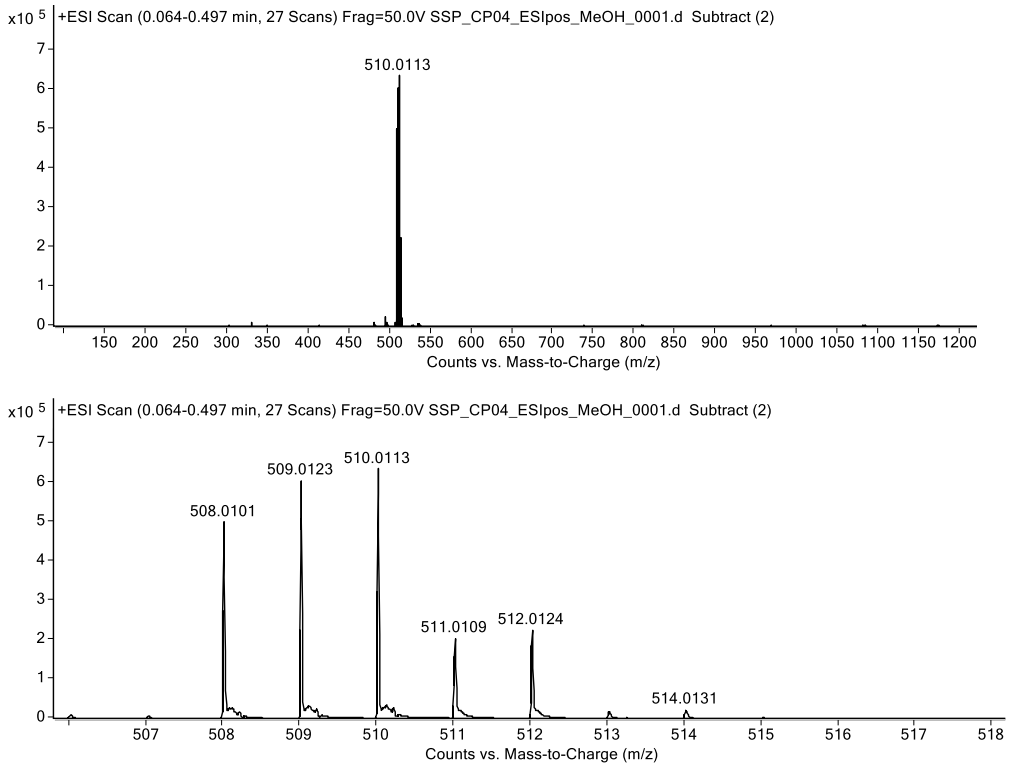

Figure S1b. Results of ESI-MS analyses of compounds **3** and **4**.

1@CB7 – positive mode, H_2O

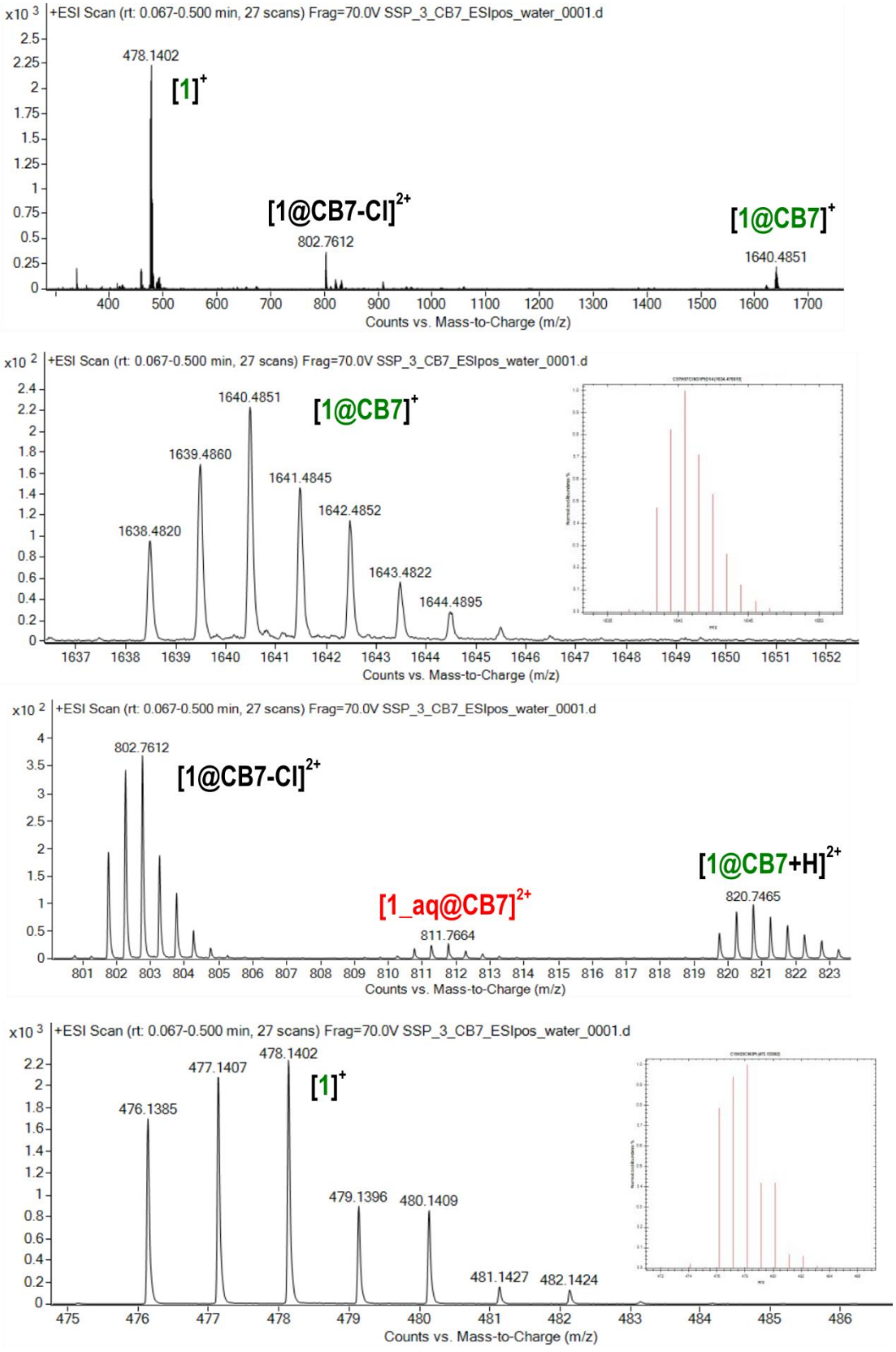

Figure S1c. Results of ESI-MS analyses of the of **1**, **1@CB7** and **1_aq@CB7**.

2@CB7 – positive mode, H_2O

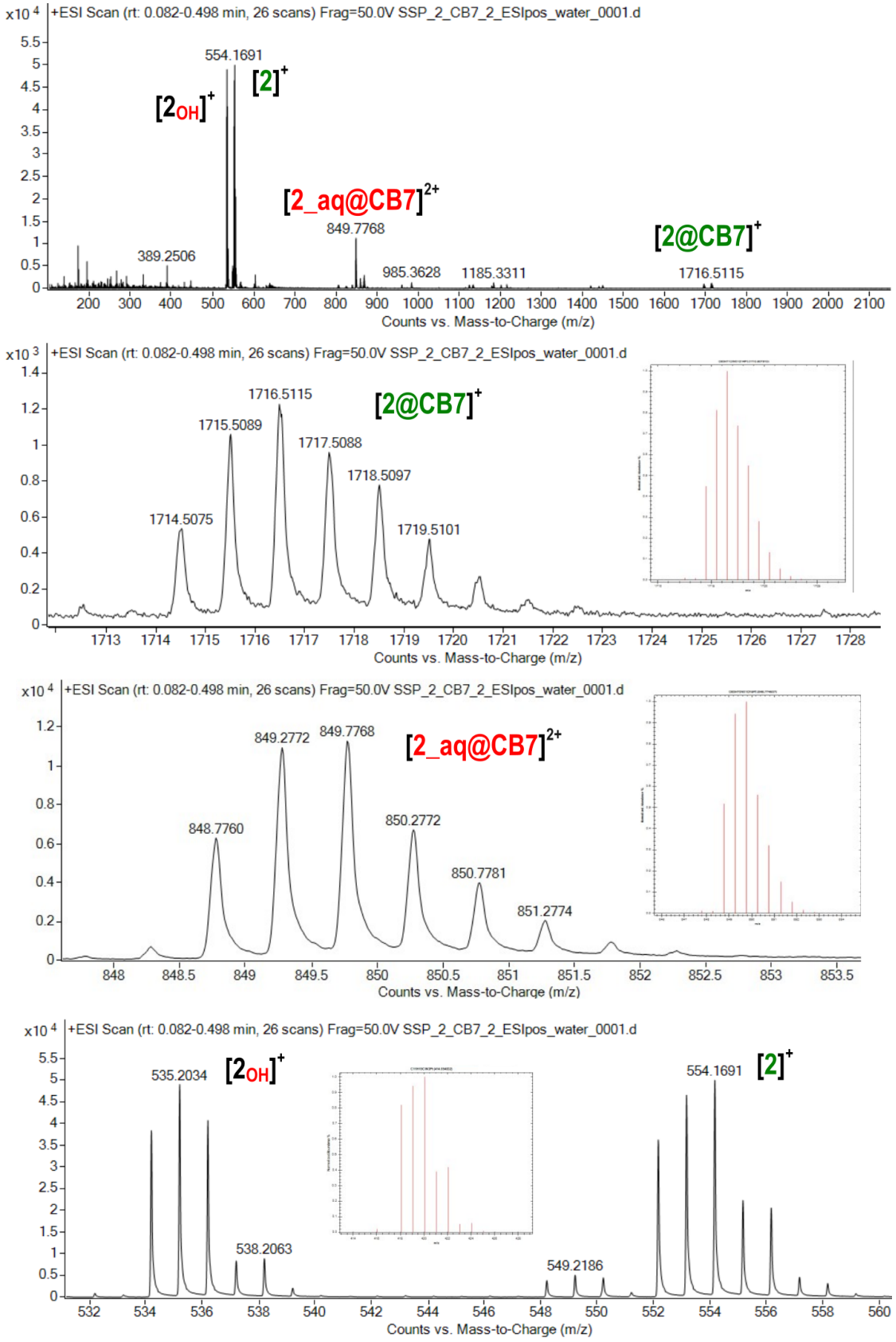

Figure S1d. Results of ESI-MS analyses of the of **2**, $\mathbf{2_{OH}}$, **2@CB7** and **2_aq@CB7**.

3@CB7 – positive mode, H_2O

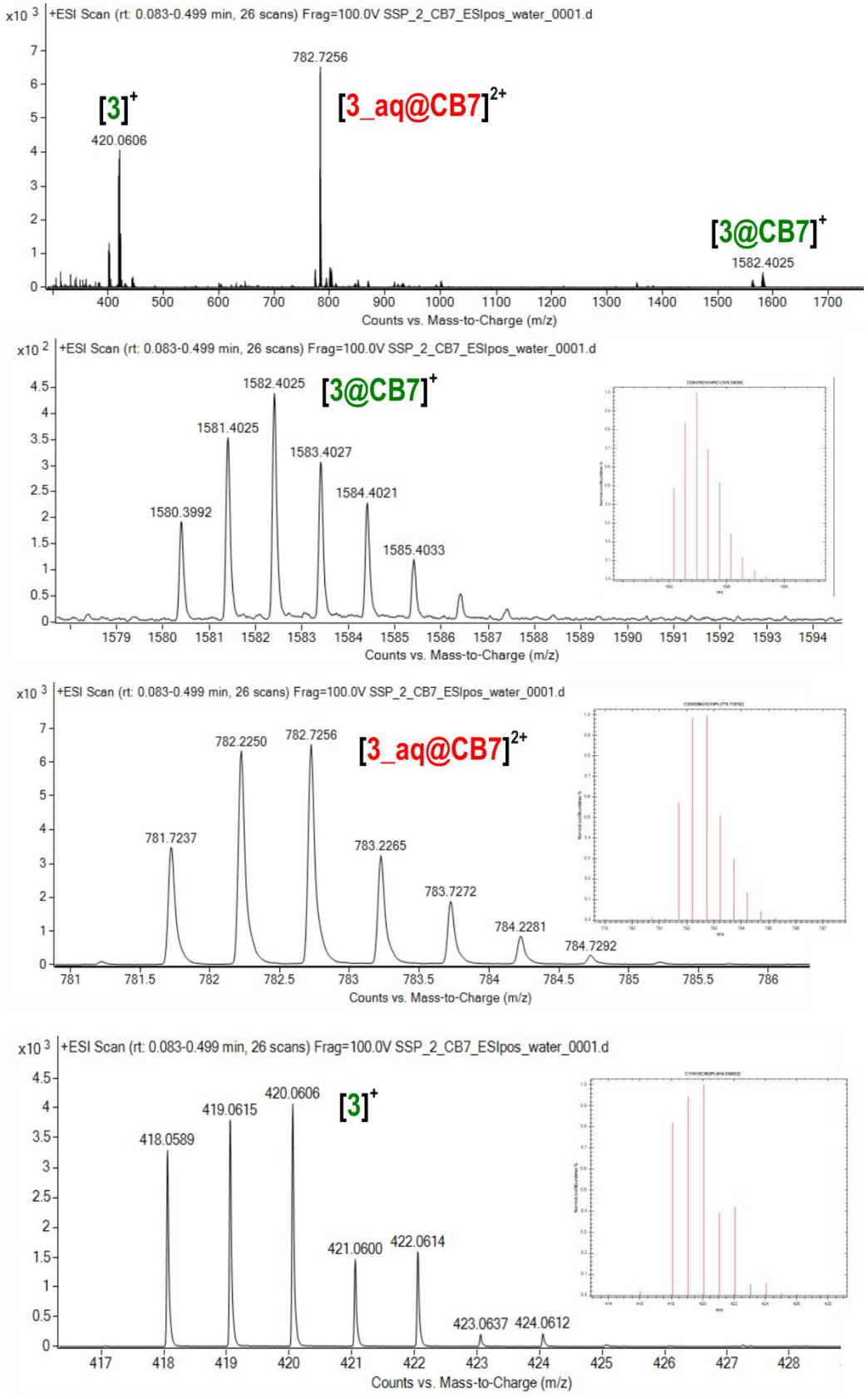

Figure S1e. Results of ESI-MS analyses of the of **3**, **3@CB7** and **3_aq@CB7**.

4@CB7 – positive mode, H_2O

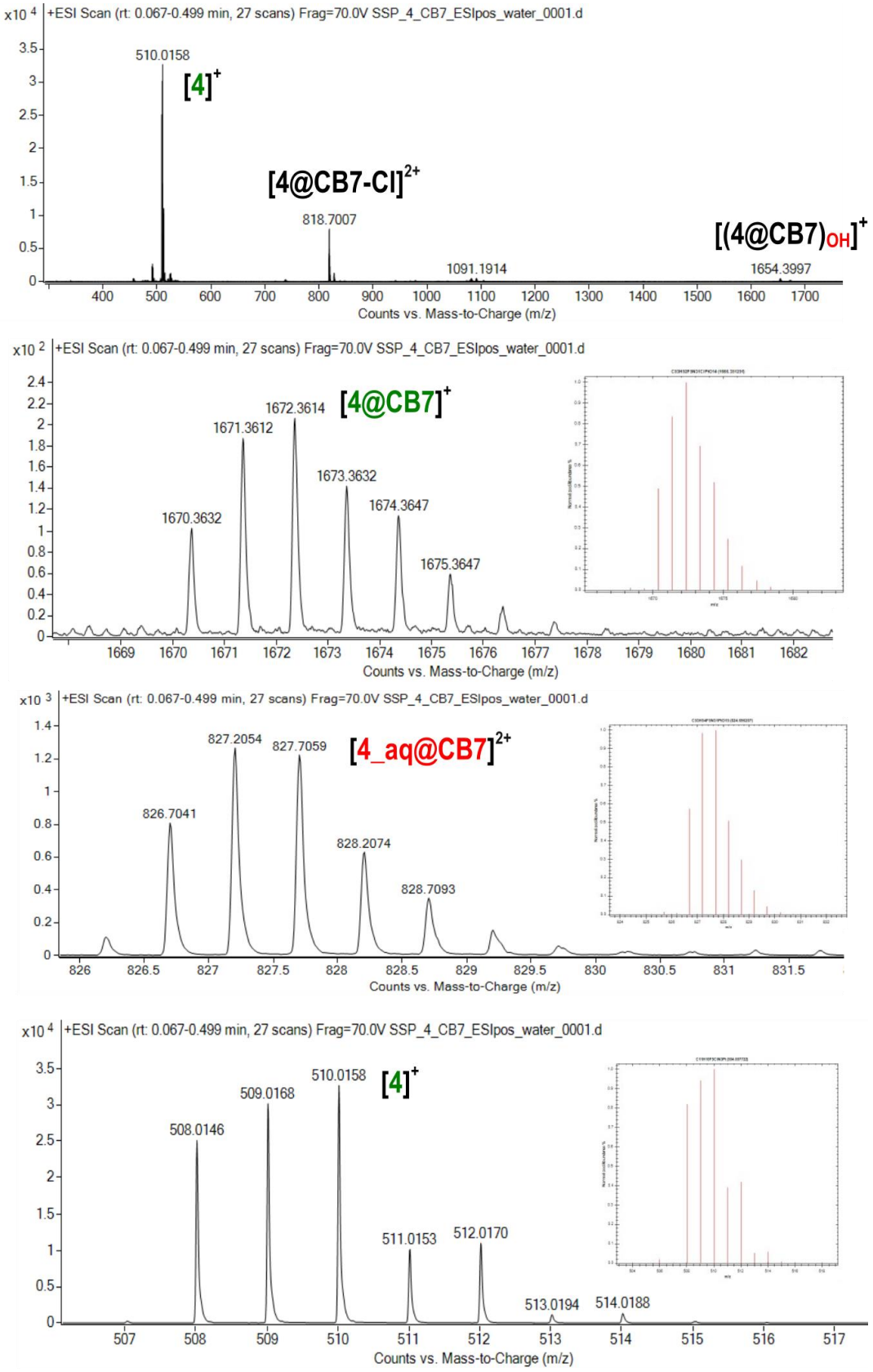

Figure S1f. Results of ESI-MS analyses of the of **4**, **4@CB7** and **4_aq@CB7**.

S3. NMR SPECTROSCOPY

S3.1. NMR Spectroscopy of Lignads

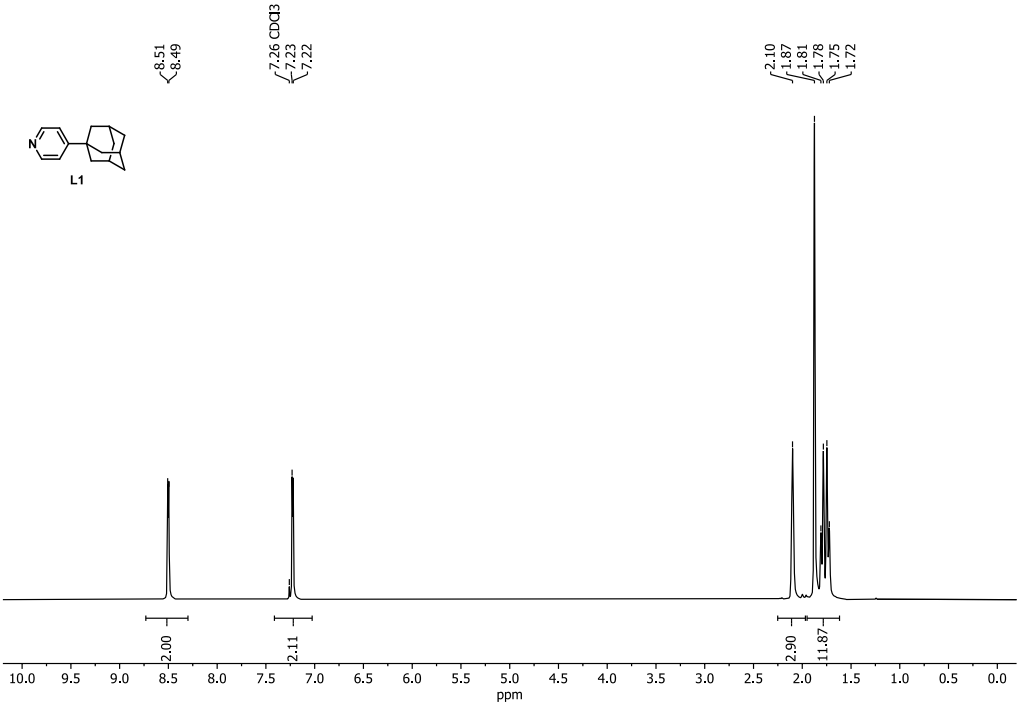

Figure S2a. ^{1}H NMR ($CDCl_3$, 500 MHz, 298 K) spectrum of **L1**.

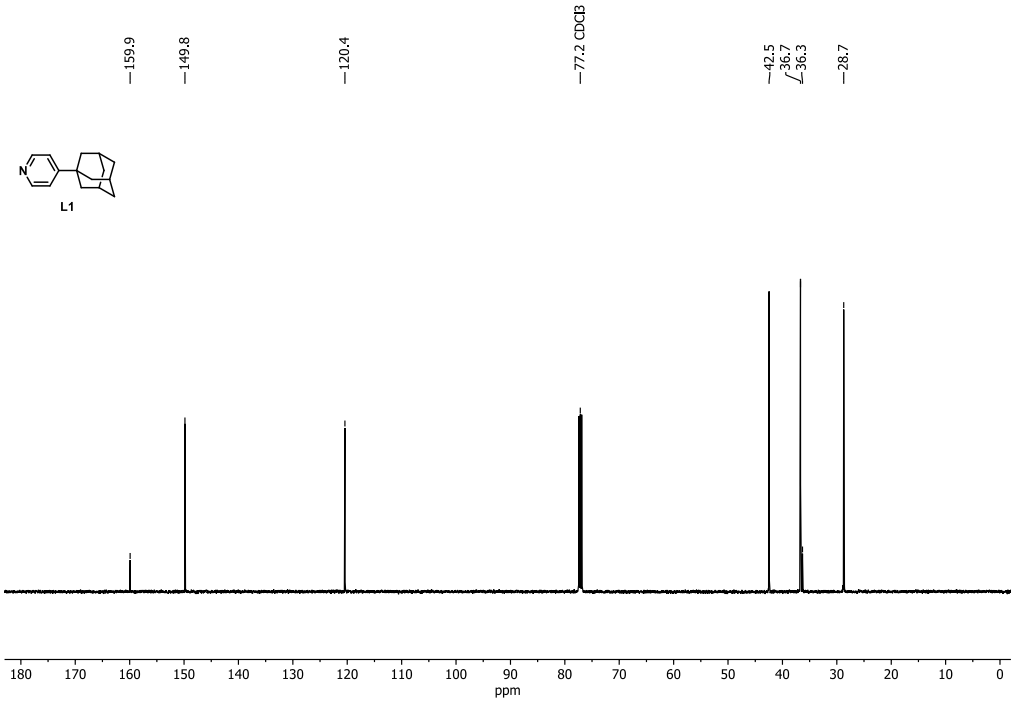

Figure S2b. ^{13}C NMR ($CDCl_3$, 126 MHz, 298 K) spectrum of **L1**.

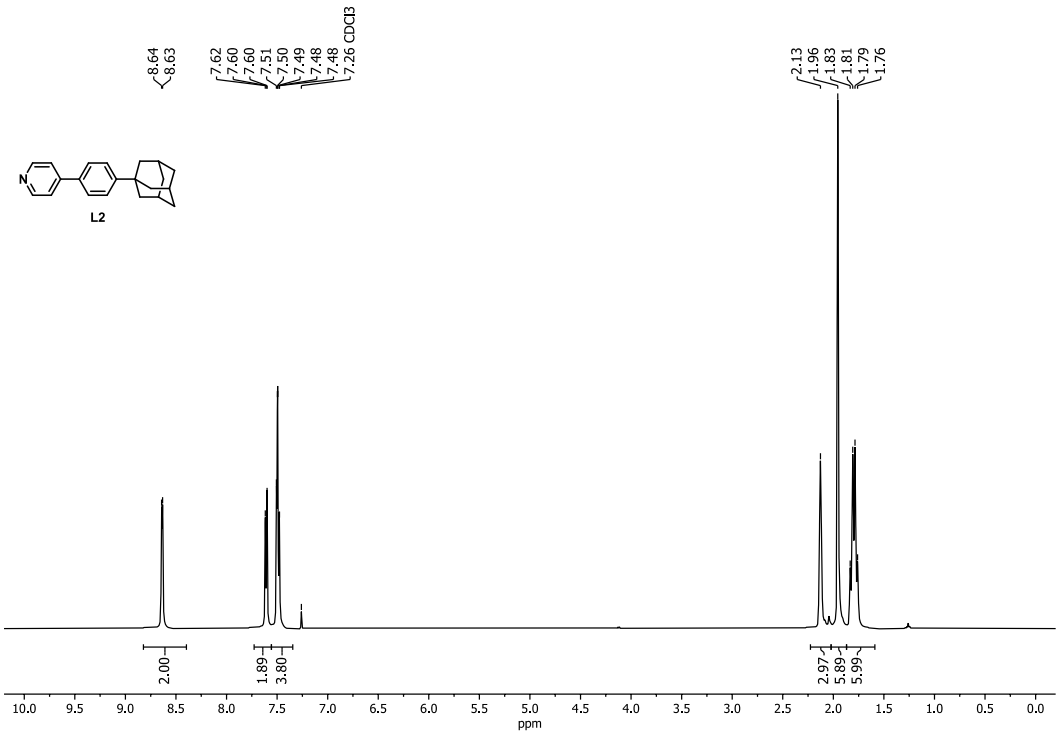

Figure S2c. ^{1}H NMR ($CDCl_3$, 500 MHz, 298 K) spectrum of **L2**.

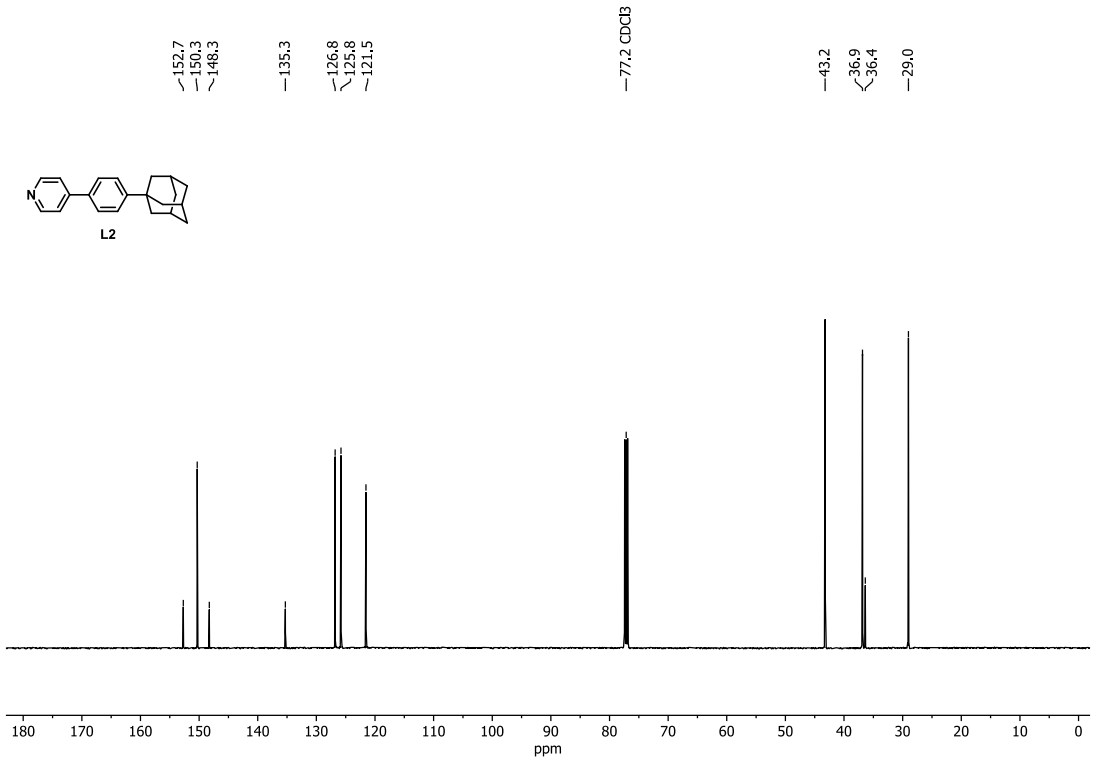

Figure S2d. ^{13}C NMR ($CDCl_3$, 126 MHz, 298 K) spectrum of **L2**.

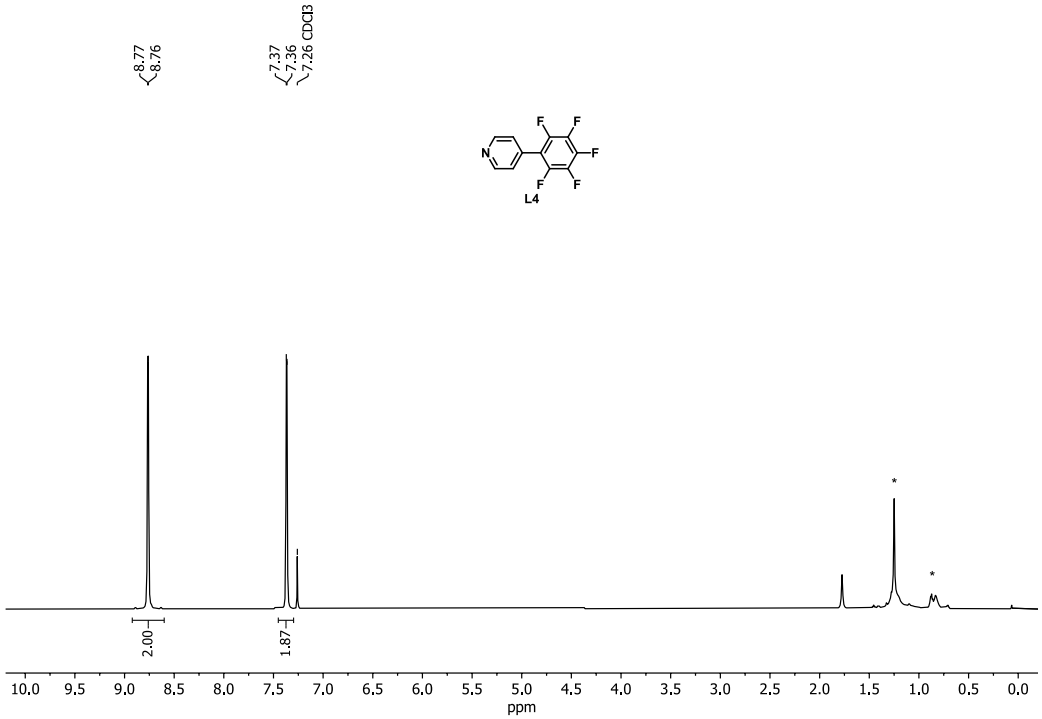

Figure S2e. ^{1}H NMR ($CDCl_3$, 700 MHz, 298 K) spectrum of **L4** (* = grease).

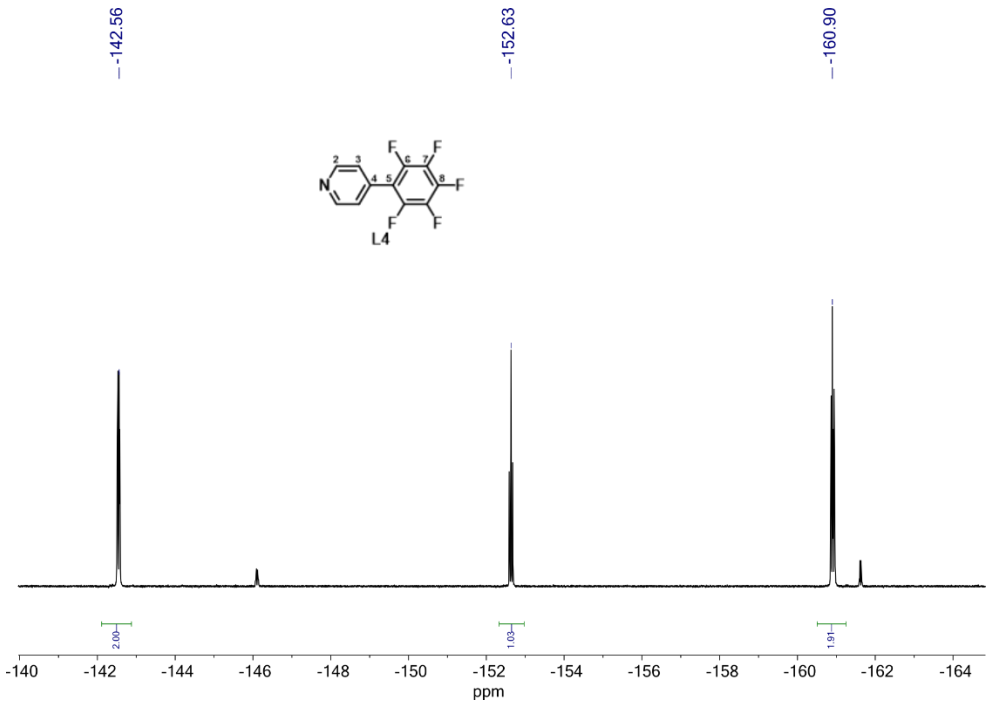

Figure S2f. ^{19}F NMR ($CDCl_3$, 470 MHz, 298 K) spectrum of **L4**.

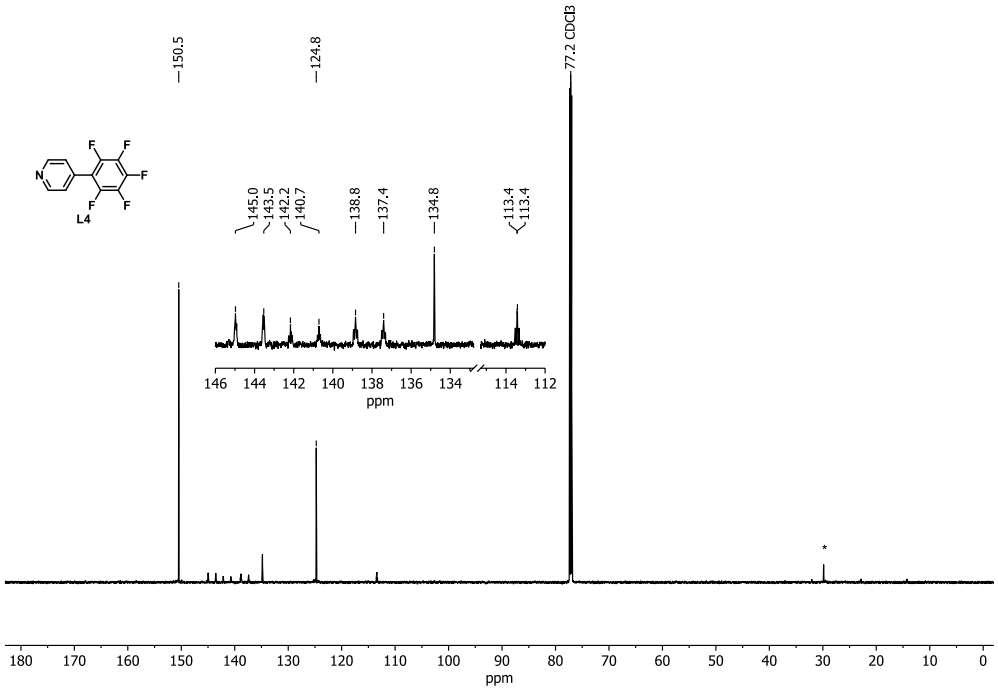

Figure S2g. ^{13}C NMR ($CDCl_3$, 176 MHz, 298 K) spectrum of **L4** (* = grease).

S3.2. NMR Spectroscopy of Platinum(II) Compounds 1-4 and Their HG Assemblies with CB7

Table S1. ^{1}H NMR chemical shifts (ppm) for compound **1**, **1_aq**, **1@CB7**, and **1_aq@CB7** measured in D_2O at 298 K. Data referenced using D_2O lock frequency.

Compound	H6	H7	H14	H15	H16a	H16b
1	8.47(d)	7.45(d)	2.01(s)	1.82(s)	1.73(d)	1.66(d)
1_aq	8.50(d)	7.52(d)	2.02(s)	1.83(s)	1.73(d)	1.66(d)
1@CB7	8.44(d)	7.57(d)	1.25(s)	1.09(s)	1.18(d)	0.93(d)
1_aq@CB7	8.48(d)	7.62(d)	1.26(s)	1.09(s)	1.19(d)	0.93(d)
Δ(**1@CB7 – 1**)	**-0.03**	**+0.12**	**-0.76**	**-0.73**	**-0.55**	**-0.73**
Δ(**1_aq@CB7 – 1_aq**)	**-0.02**	**+0.10**	**-0.76**	**-0.74**	**-0.54**	**-0.73**

Table S2. ^{1}H NMR chemical shifts (ppm) for compound **2**, **2_aq**, **2@CB7**, and **2_aq@CB7** measured in D_2O at 298 K. Data referenced using D_2O lock frequency.

Compound	H6	H7	H14	H15	H16a	H16b
2	8.61(d)	7.72(d)	2.01(s)	1.87(s)	1.73(d)	1.69(d)
2_aq	8.64(d)	7.77(d)	2.02(s)	1.88(s)	1.74(d)	1.69(d)
2@CB7	8.60(br)	7.83(d)	1.24(s)	1.17(s)	1.15(d)	0.97(d)
2_aq@CB7	8.64(d)	7.91(d)	1.26(s)	1.18(s)	1.16(d)	0.98(d)
Δ(**2@CB7 – 2**)	**-0.01**	**+0.11**	**-0.77**	**-0.70**	**-0.58**	**-0.72**
Δ(**2_aq@CB7 – 2_aq**)	**-0.00**	**+0.14**	**-0.76**	**-0.70**	**-0.58**	**-0.71**

Table S3. ^{1}H NMR chemical shifts (ppm) for compound **3**, **3_aq**, **3@CB7**, and **3_aq@CB7** measured in D_2O at 298 K. Data referenced using D_2O lock frequency.

Compound	H6	H7	H10	H11	H12
3	8.64(d)	7.75(d)	7.77(m)	7.52-7.53(m)	7.52-7.53(m)
3_aq	8.67(d)	7.81(d)	7.78(m)	7.53-7.54(m)	7.53-7.54(m)
3@CB7	8.54(d)	7.31(d)	6.75(d)	6.67(t)	6.93(t)
3_aq@CB7	8.55(d)	7.04(d)	6.67(d)	6.94(t)	7.09(t)
Δ(**3@CB7 – 3**)	**-0.10**	**-0.44**	**-1.02**	**-0.86**	**-0.59**
Δ(**3_aq@CB7 – 3_aq**)	**-0.12**	**-0.71**	**-1.11**	**-0.58**	**-0.43**

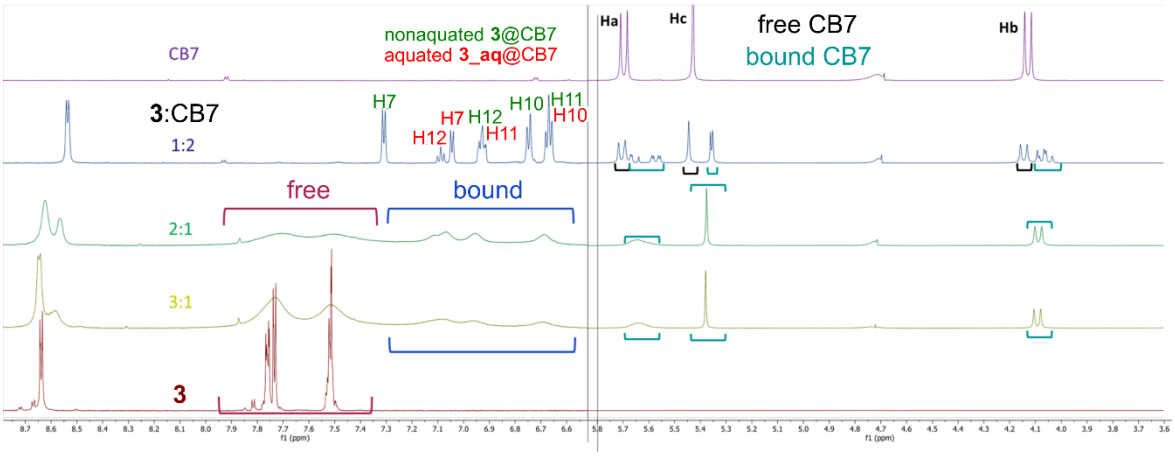

Figure S3. ^{1}H NMR spectra recorded for different molar ratios of compound **3**/**3_aq** and CB7 (measured in D_2O at 293K). The fully encapsulated ligand **3** shows sharp signals at 1:2 ratio, whereas the excess of the ligand leads to a line broadening because of faster exchange process between free and bound forms.

Table S4. ^{1}H and ^{19}F NMR chemical shifts (ppm) for compound **4**, **4_aq**, **4@CB7**, and **4_aq@CB7** measured in D_2O at 298 K. Data referenced using D_2O lock frequency.

$^{1}H/^{19}F$ NMR [ppm]	H6	H7	F10	F11	F12
4	8.78(d)	7.63(d)	-143.36(d)	-161.90(m)	-152.03(t)
4_aq	8.81(d)	7.70(d)	-143.36(d)	-161.80(m)	-151.78(t)
4@CB7	8.65(d)	6.79(br)	-145.61(br)	-155.66(br)	-152.19(t)
4_aq@CB7	8.49(d)	6.48(d)	-142.88(d)	-154.84(m)	-152.38(t)
Δ(4@CB7-4)	**-0.13**	**-0.84**	**-2.25**	**+6.24**	**-0.16**
Δ(4_aq@CB7-4_aq)	**-0.32**	**-1.22**	**+0.47**	**+6.96**	**-0.60**

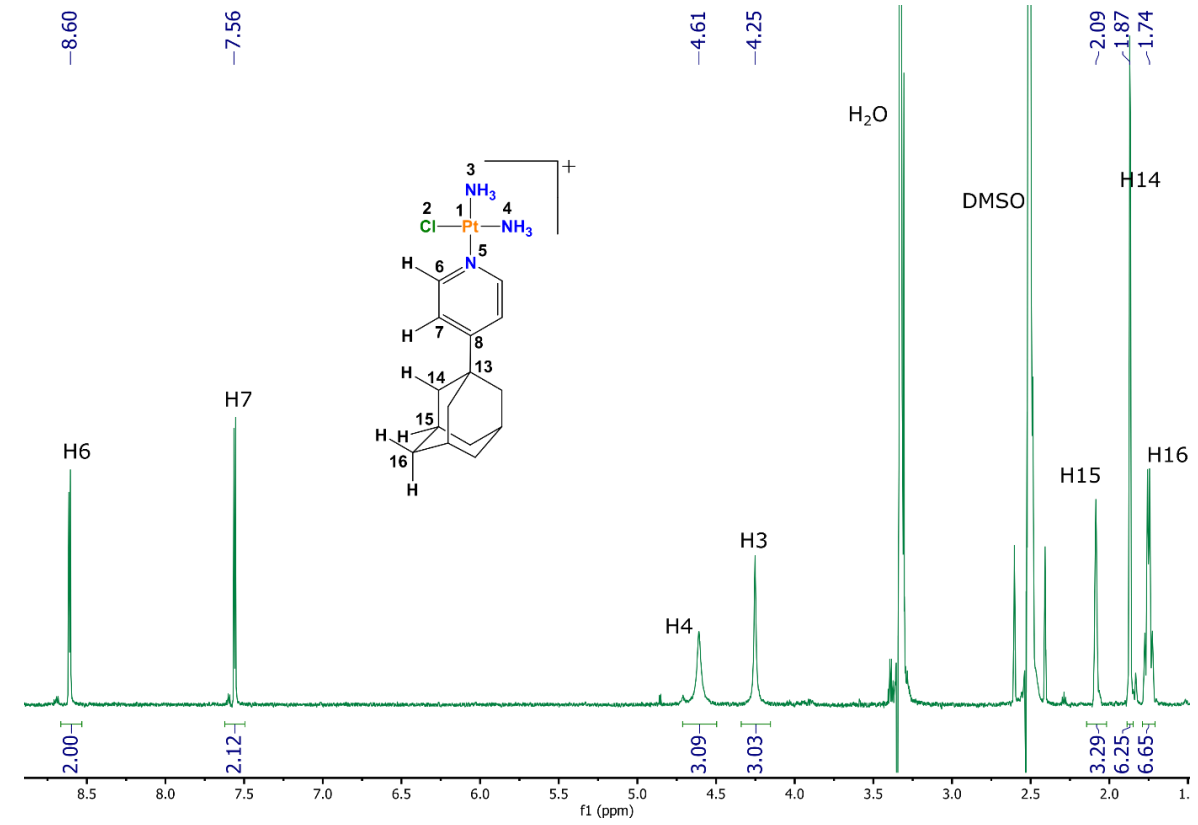

Figure S4. ^{1}H NMR spectrum of compound **1** in DMSO-d_6 at 298K.

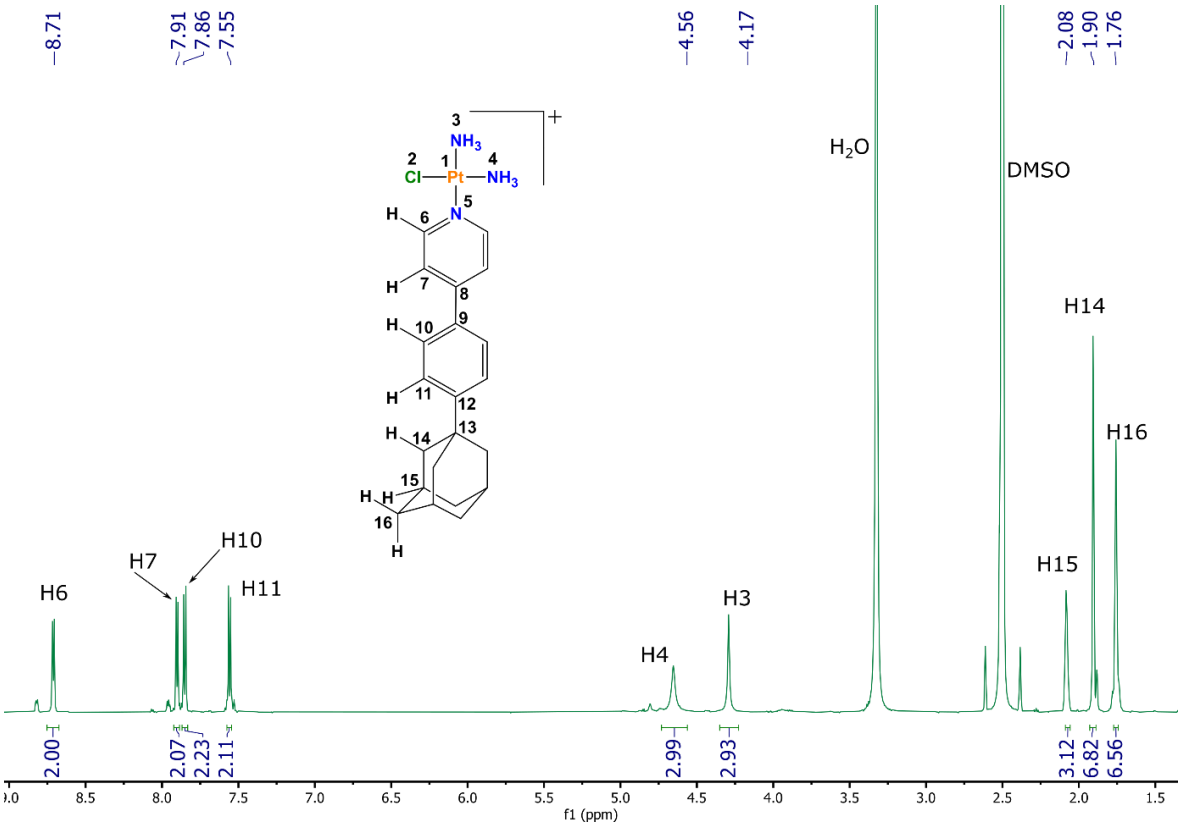

Figure S5. ^{1}H NMR spectrum of compound **2** in DMSO-d_6 at 298K.

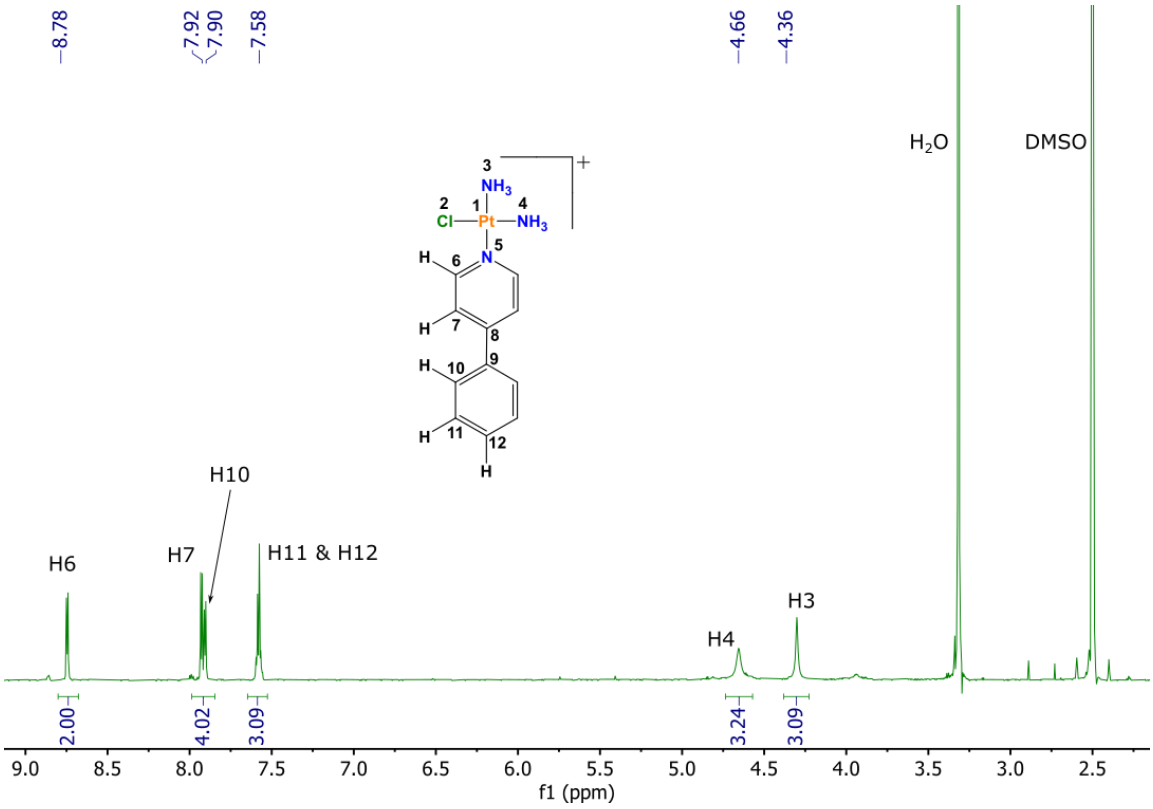

Figure S6. ^{1}H NMR spectrum of compound **3** in DMSO-d_6 at 298K.

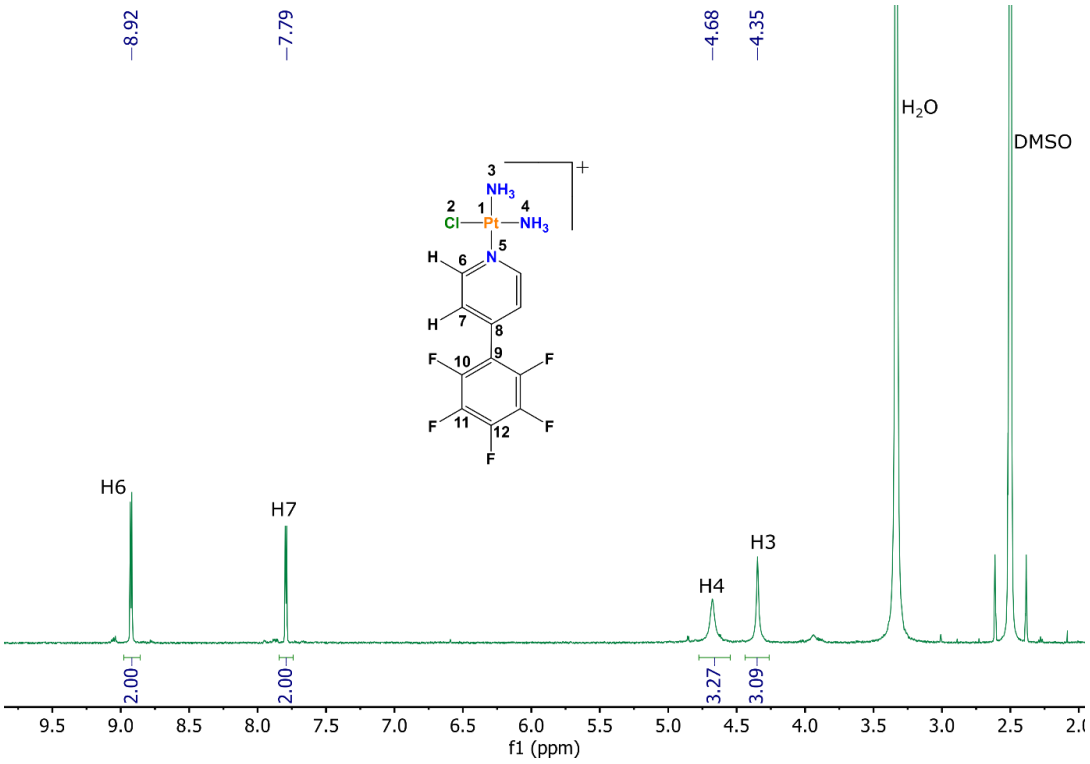

Figure S7. ^{1}H NMR spectrum of compound **4** in DMSO-d_6 at 298K.

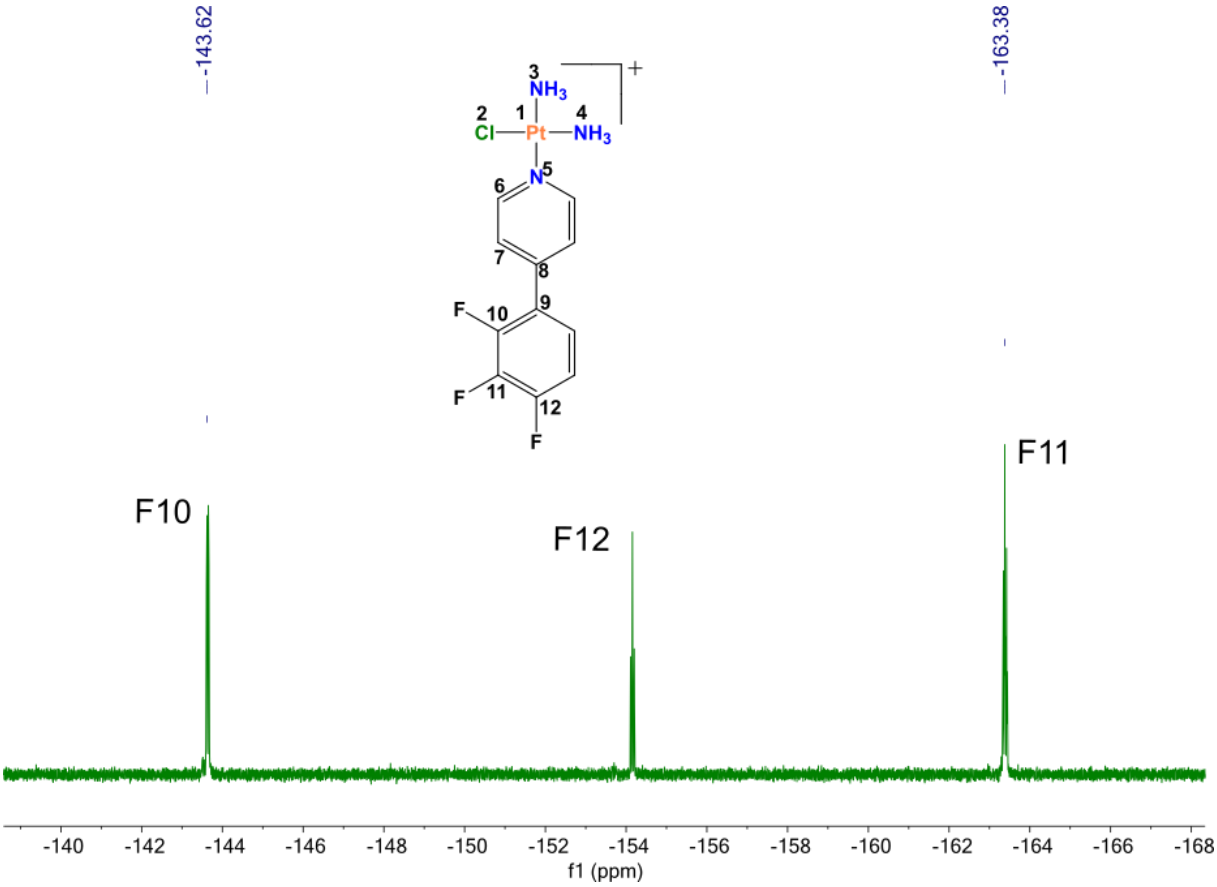

Figure S8. ^{19}F NMR spectrum of compound **4** in DMF-d_7 at 298K.

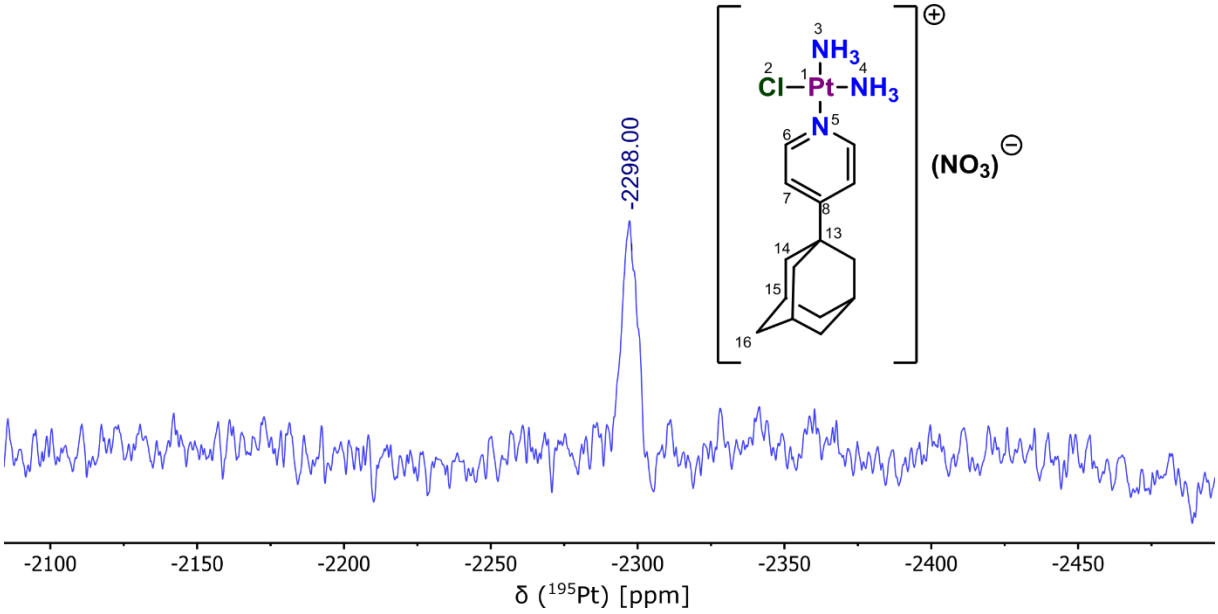

Figure S9. ^{195}Pt NMR spectrum of compound **1** in D_2O at 298K.

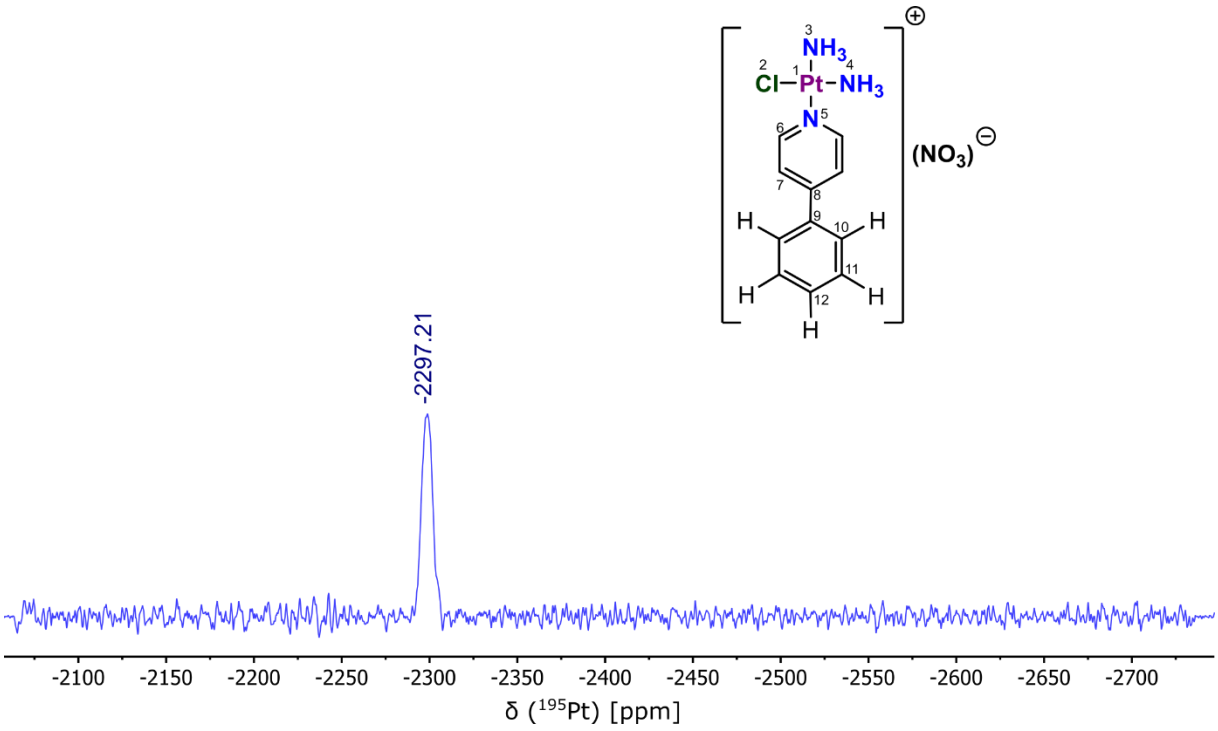

Figure S10. ^{195}Pt NMR spectrum of compound **3** in D_2O at 298K.

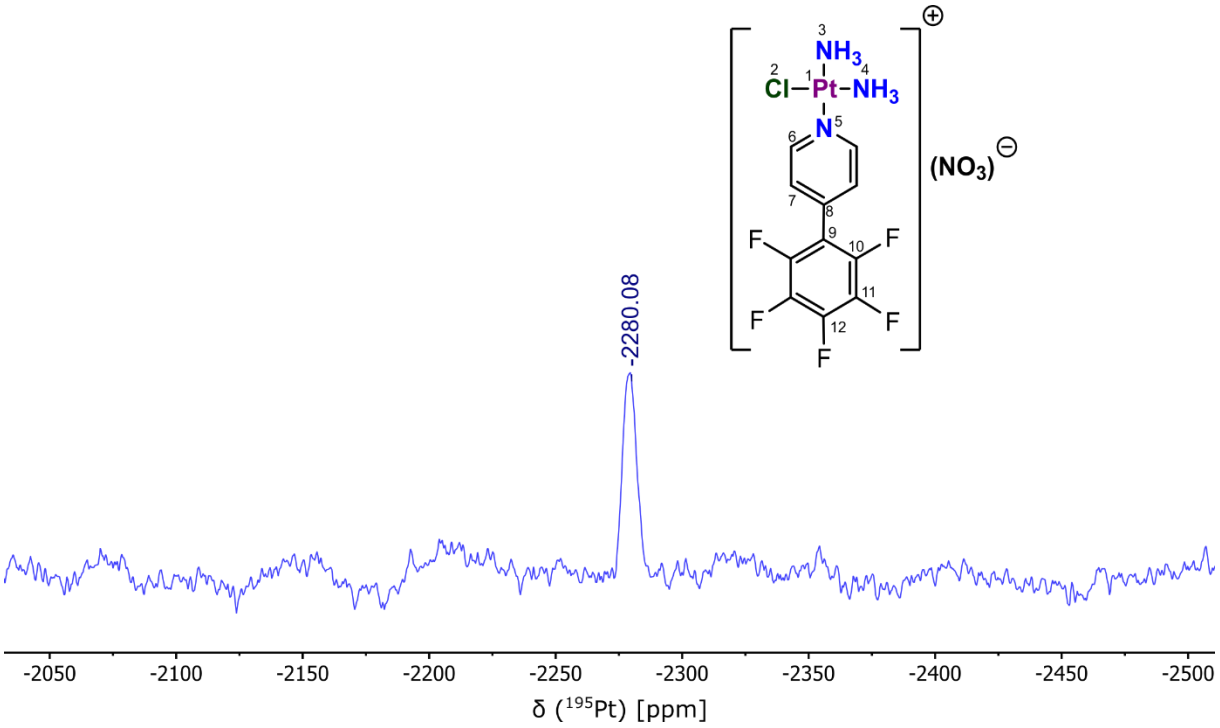

Figure S11. ^{195}Pt NMR spectrum of compound **4** in D_2O at 298K.

^{195}Pt NMR resonances of compounds **1**, **3**, and **4** are significantly broadened because of the large chemical shift anisotropy (CSA). Therefore, it takes 24-48 hrs (1mM solutions) to accumulate ^{195}Pt NMR signals with sufficient signal-to-noise ratio; for less populated forms (**1_aq@CB7**, **4@CB7**) and low-concentration sample (poor solubility of **2@CB7** in water) no ^{195}Pt NMR resonances were detected. Because of the long accumulation period and lower sensitivity, ^{195}Pt NMR provide information about the dominant (thermodynamically stable) forms. For the HG systems of **1** and **4** where only one form dominates after 24 hours, we obtained a single ^{195}Pt NMR resonance (Figure S12) corresponding to **1@CB7** (approx. -2290 ppm) and **4_aq@CB7** (approx. -2070 ppm), respectively. However, for two approximately equally populated HG assemblies of compound **3**, two ^{195}Pt NMR signals at -2290 ppm (**3@CB7**) and -2080 ppm (**3_aq@CB7**) were obtained. This observation is in excellent agreement with the ^{1}H NMR experiments discussed in detail in the main text.

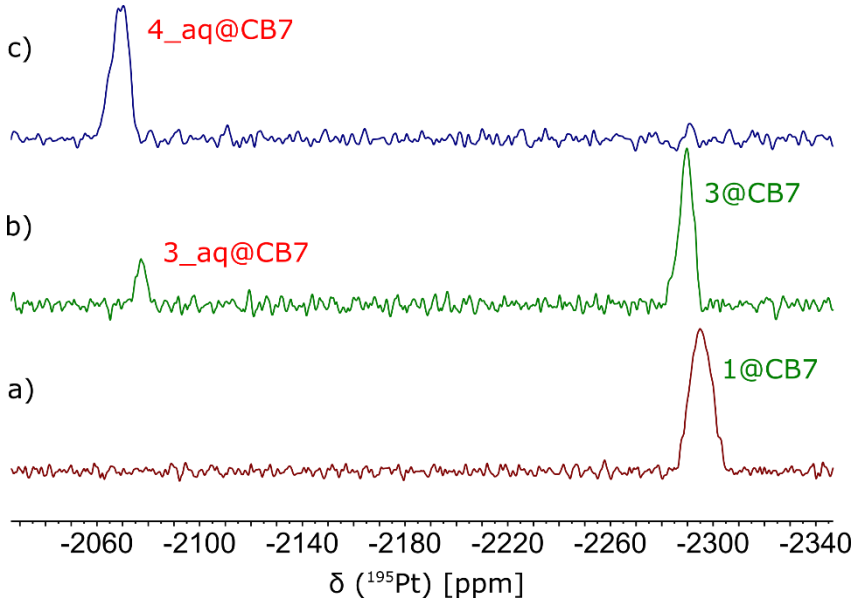

Figure S12. ^{195}Pt-NMR spectrum of a) **1@CB7**, b) mixture of **3@CB7** and **3_aq@CB7**, and c) **4_aq@CB7**.

Stability of Compound 1 in D_2O:

Commercially available CB7 contains some amount of HCl and pH ~ 3 of its solution indicates that it contains approximately 1 mM chloride (considering HCl the only source of H^+). This concentration of chlorides can influence the Pt-Cl ↔ Pt-OH_2 equiulibria. Therefore we checked the stability of the free compound **1** under similar conditions. Solid compound **1** (0.54 mg, 1mmol) was dissolved in 1 mL solution of D_2O adjusted to pH ~ 2.7 by using DCl solution (Figure S13). We observed very small amount (approx. 10%) of aquated form appearing over 24 hours. Then we increased the pH to 7 using $NaHCO_3$ and monitored the aquation process (Figure S14). This shows little to no change in degree of conversion to the aquated form meaning that pH has marginal effect on the aquation of the Pt-Cl bond.

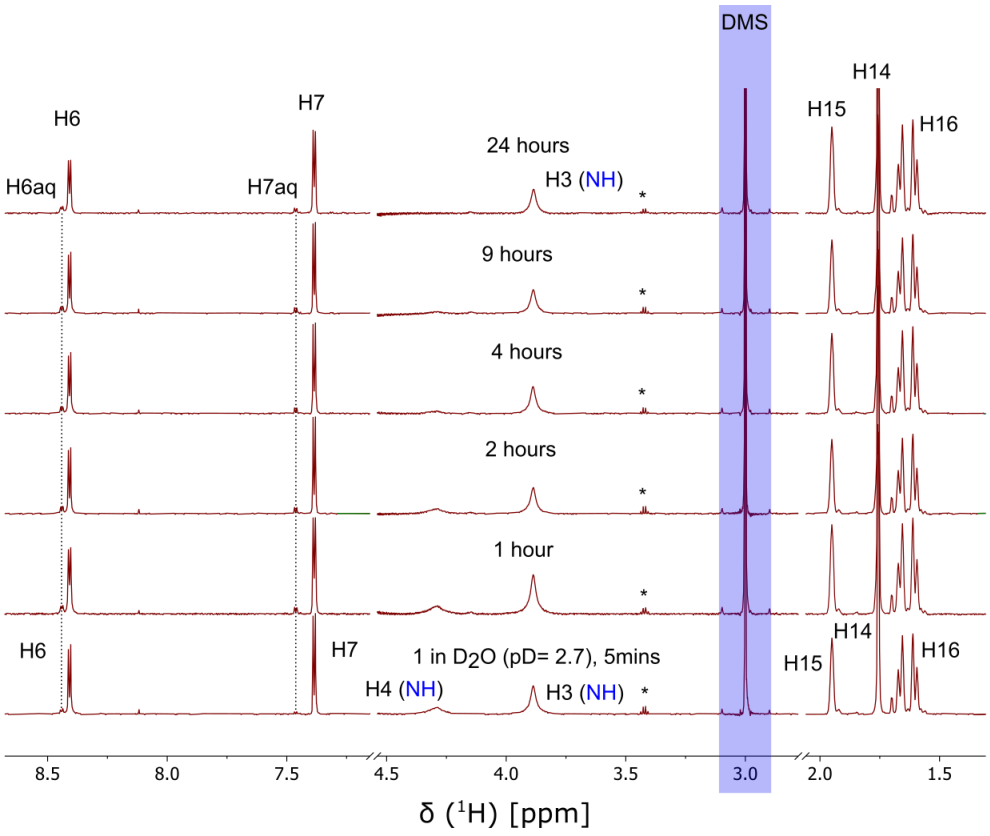

Figure S13. ^{1}H NMR spectra of compound **1** dissolved in D_2O and acidity adjusted to pD~3 by using DCl.

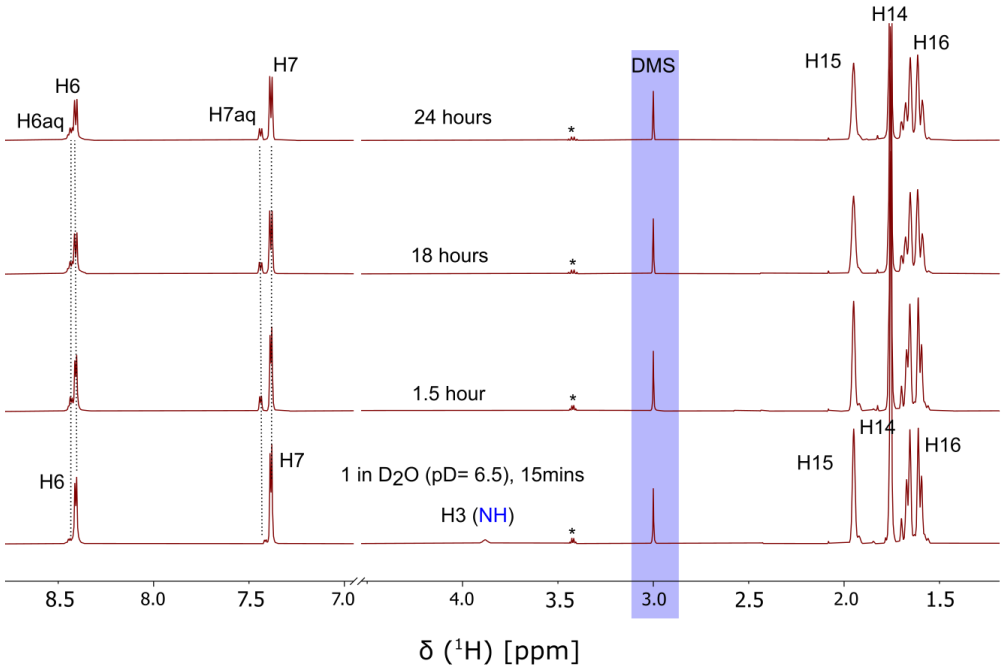

Figure S14. ^{1}H NMR spectra of compound **1** dissolved in D_2O and acidity adjusted to pD~7 (first pD~3 by using DCl followed by $NaHCO_3$ to pD~7).

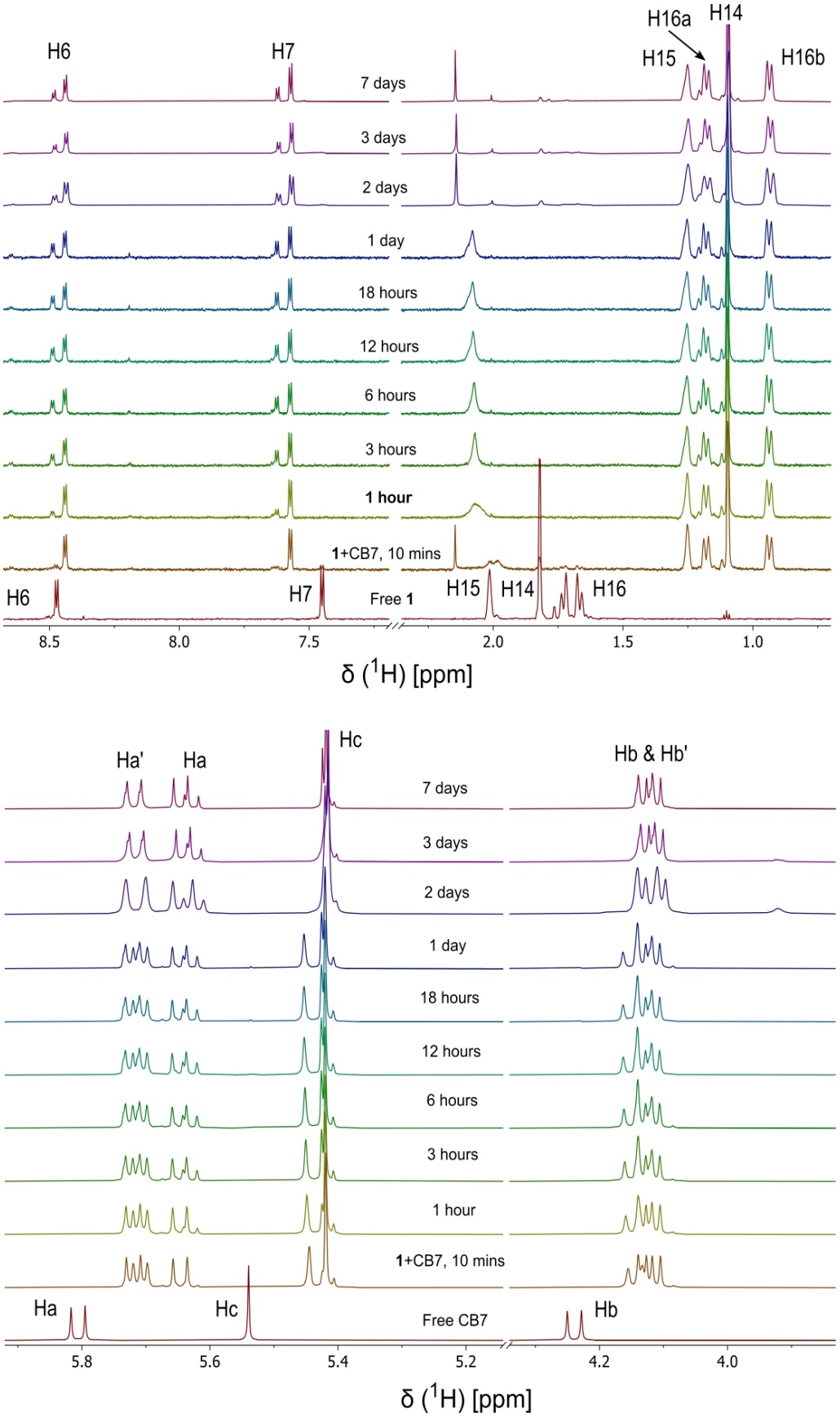

Figure S15. ^{1}H NMR spectra of **1@CB7** (guest, top; host, bottom) measured at several different times of aquation in water (pD~4) at 298 K.

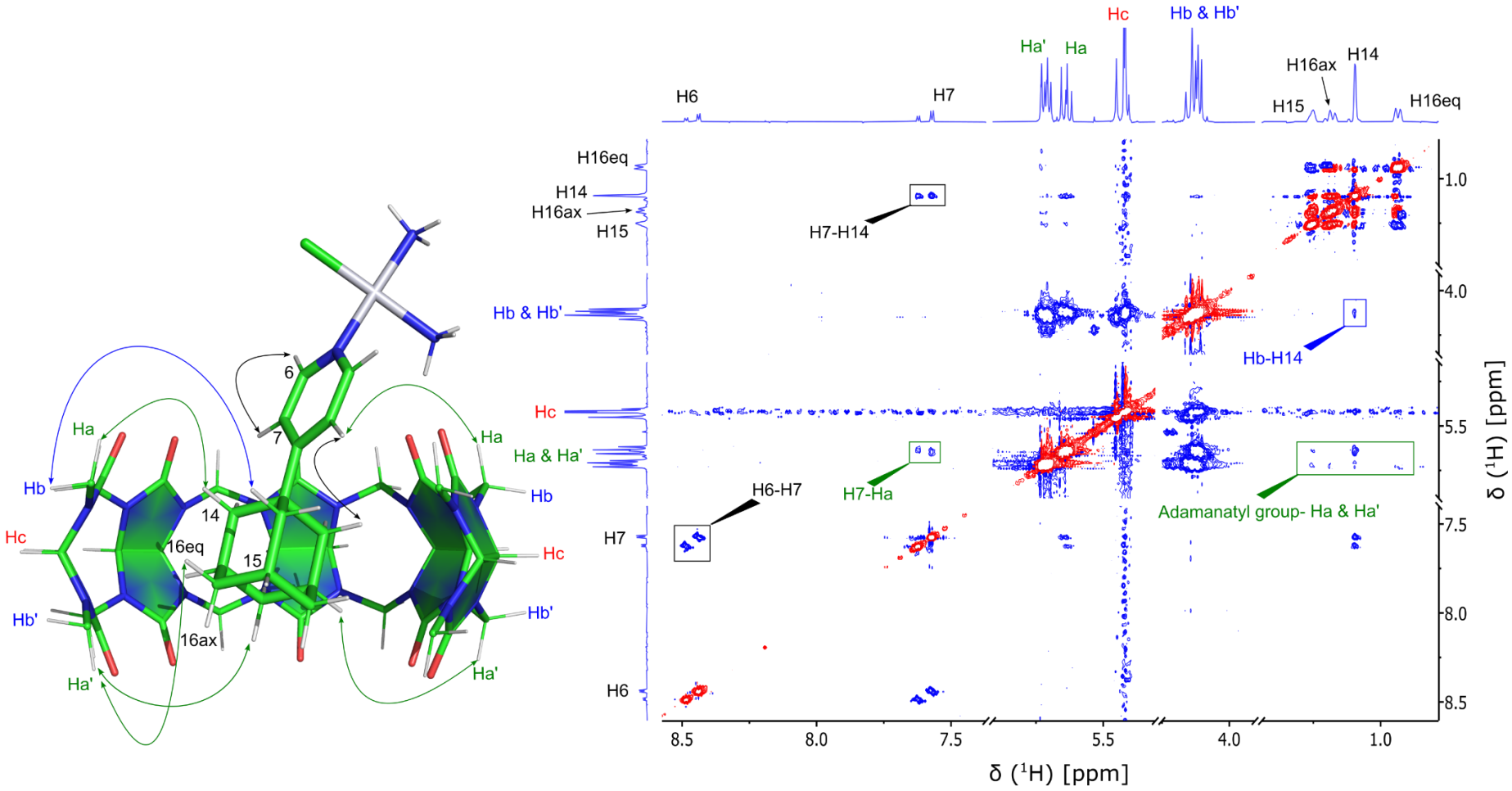

Figure S16. ^{1}H-^{1}H ROESY spectrum of **1@CB7/1_aq@CB7** measured in water at 298 K.

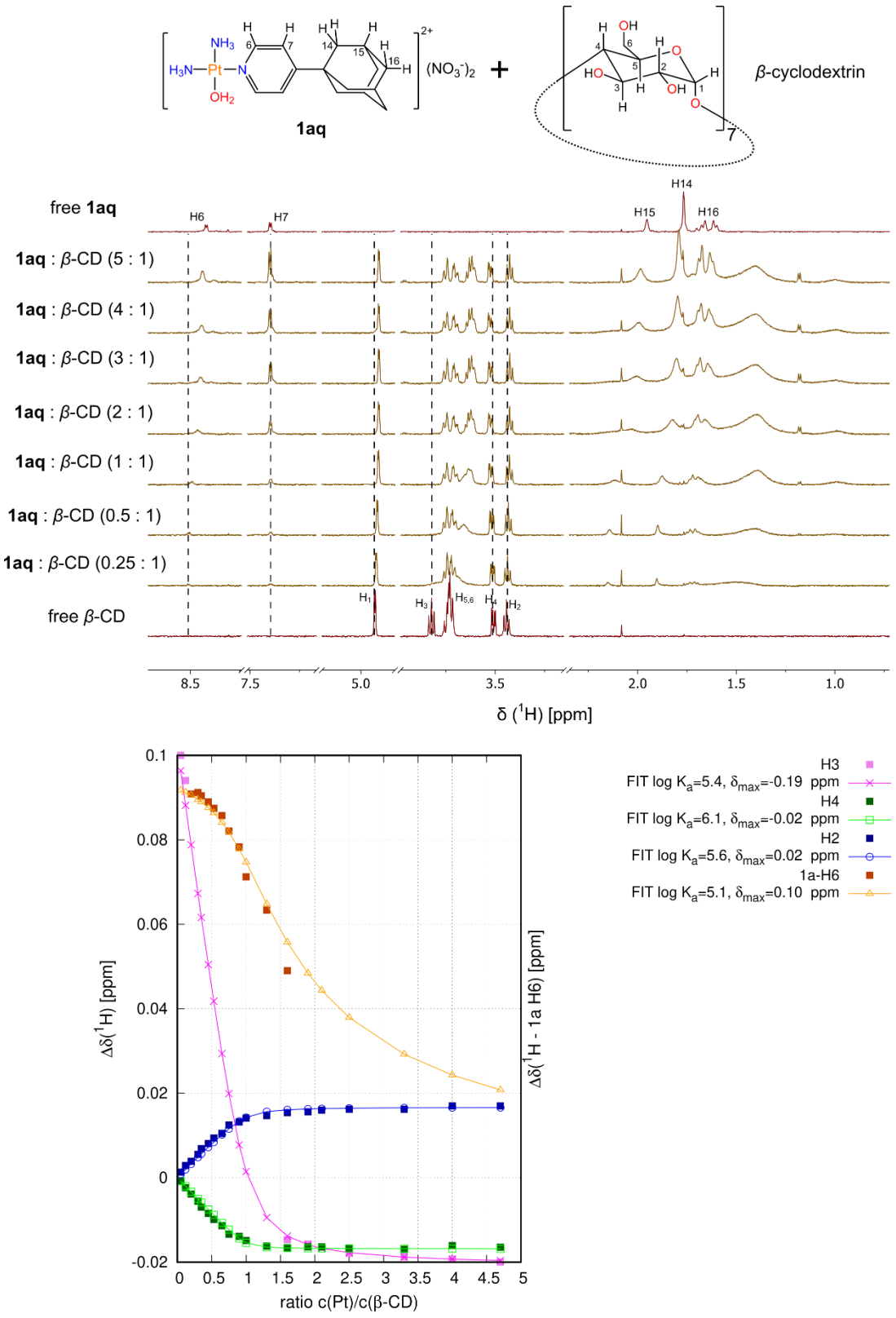

Figure S17a. Record of ^{1}H NMR titration of compound **1_aq** into *β*-CD (c = 0.1 mM) measured in D_2O at 298K. Resulting estimate of the binding constats is logK_a ~ 5.7.

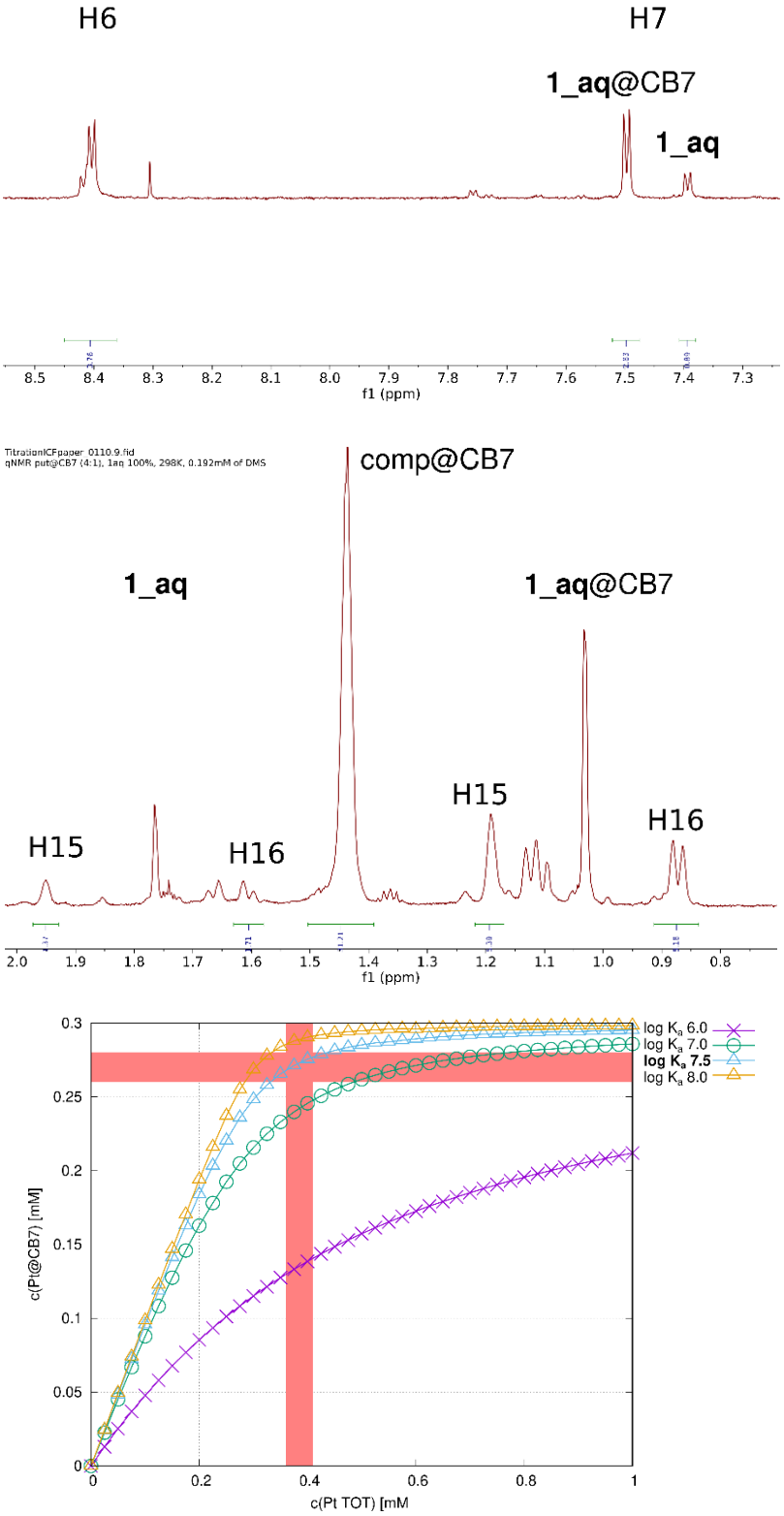

Figure S17b. ^{1}H NMR of compound **1_aq** (0.36 mM) mixed with CB7 (0.34 mM) in the presence of putrescine dihydrochloride as a competitor (1.41 mM, logK_a~5.5) measured in D_2O at 298 K. Plot in the bottom shows simulated dependence of the concentration of **1_aq** bound in CB7 as a function of total **1_aq** concentration and various binding constants.

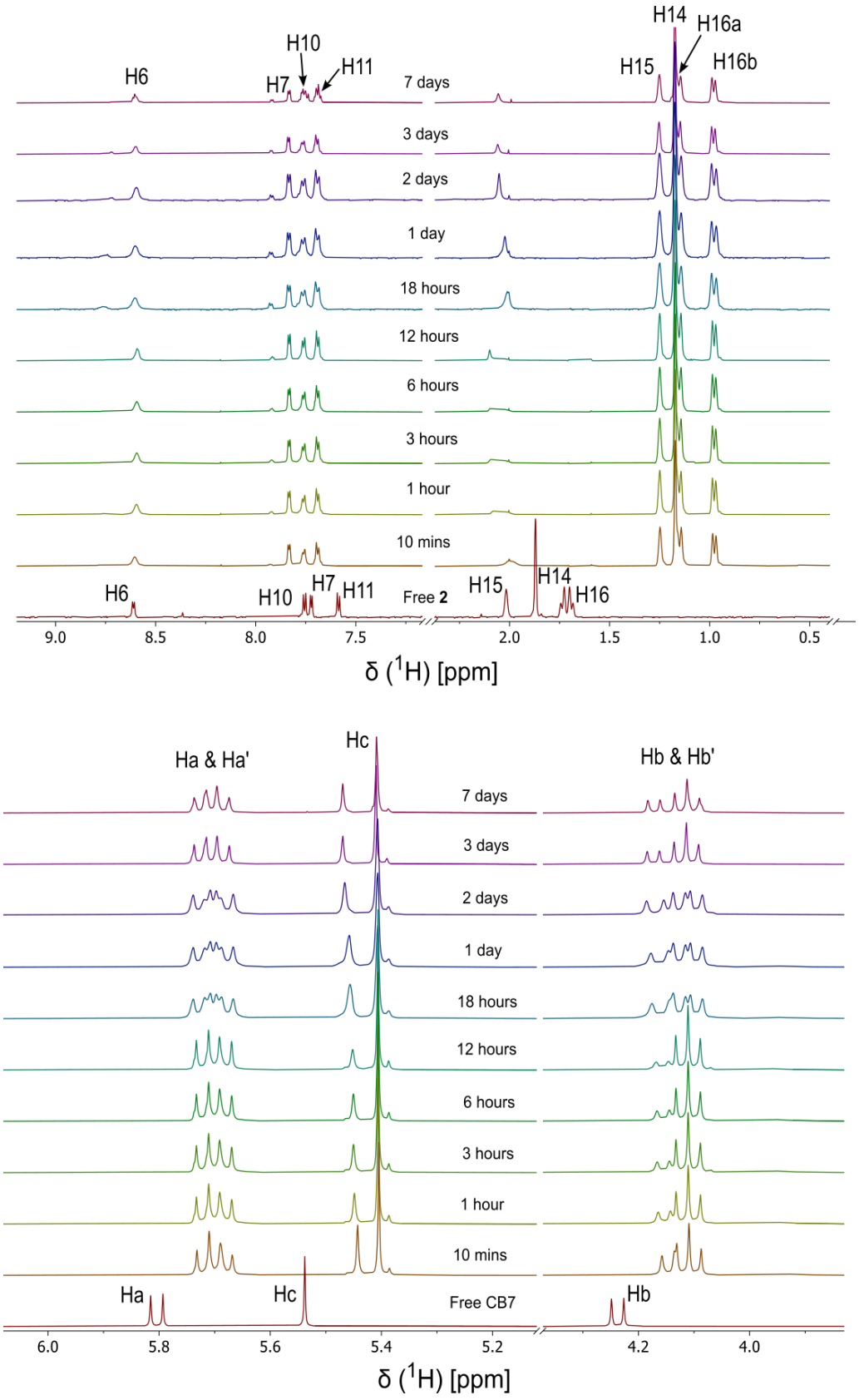

Figure S18. ^{1}H NMR spectra of **2@CB7** (guest, top; host, bottom) measured at several different times of aquation in water at 298 K.

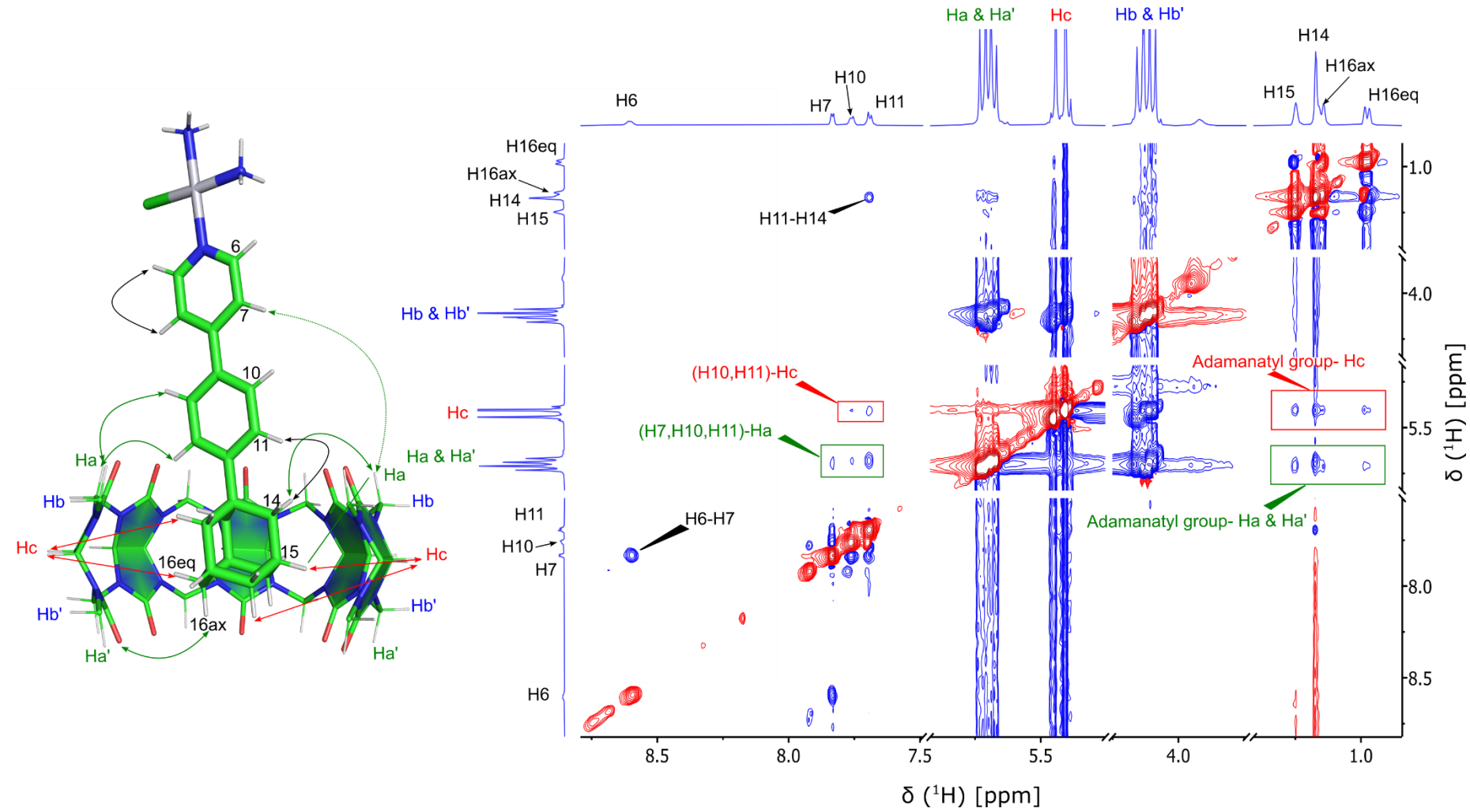

Figure S19. ^{1}H-^{1}H ROESY spectrum of **2@CB7** measured in water at 298K.

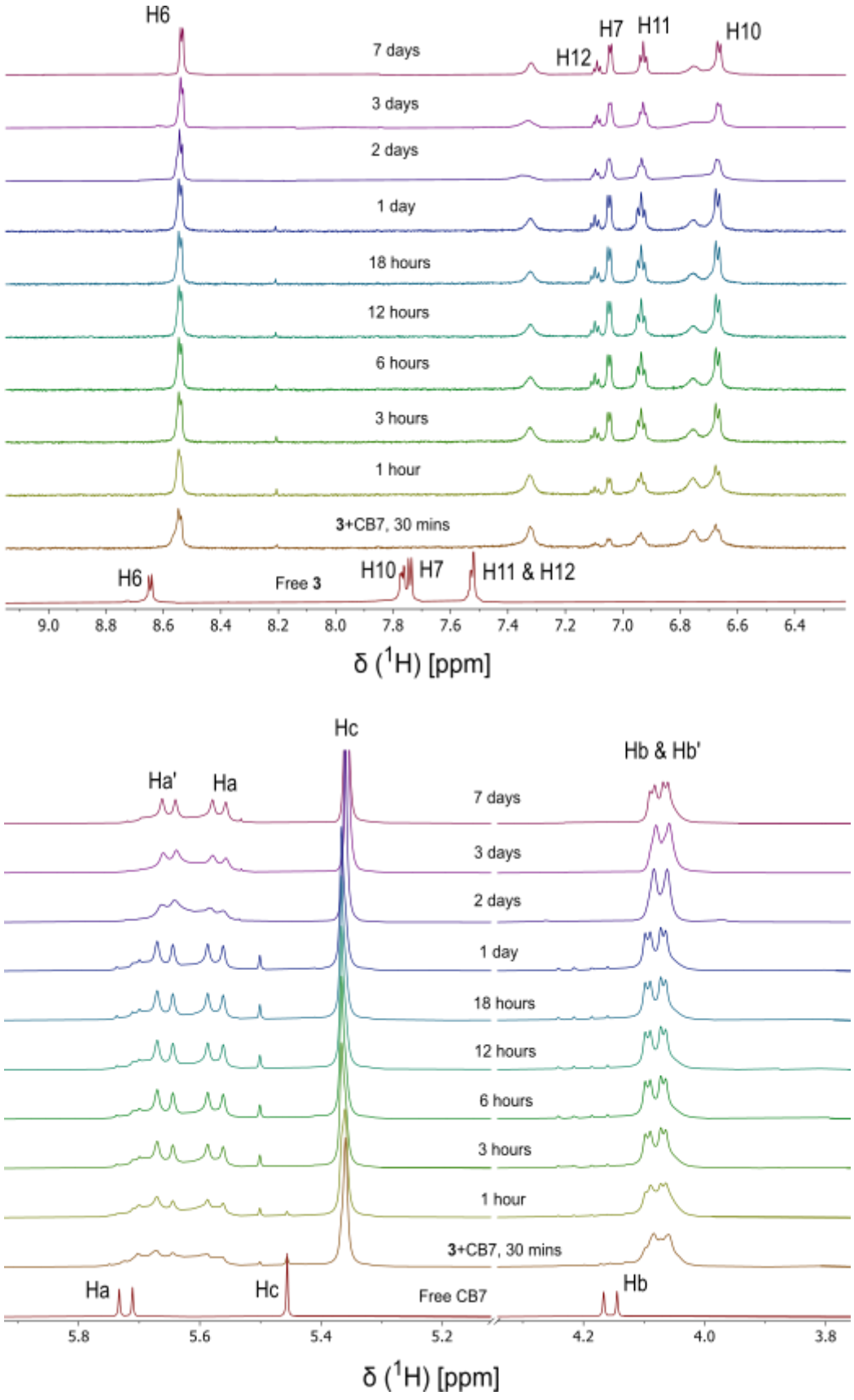

Figure S20. ^{1}H NMR spectra of **3@CB7** (guest, top; host, bottom) measured at several different times of aquation in water at 298 K.

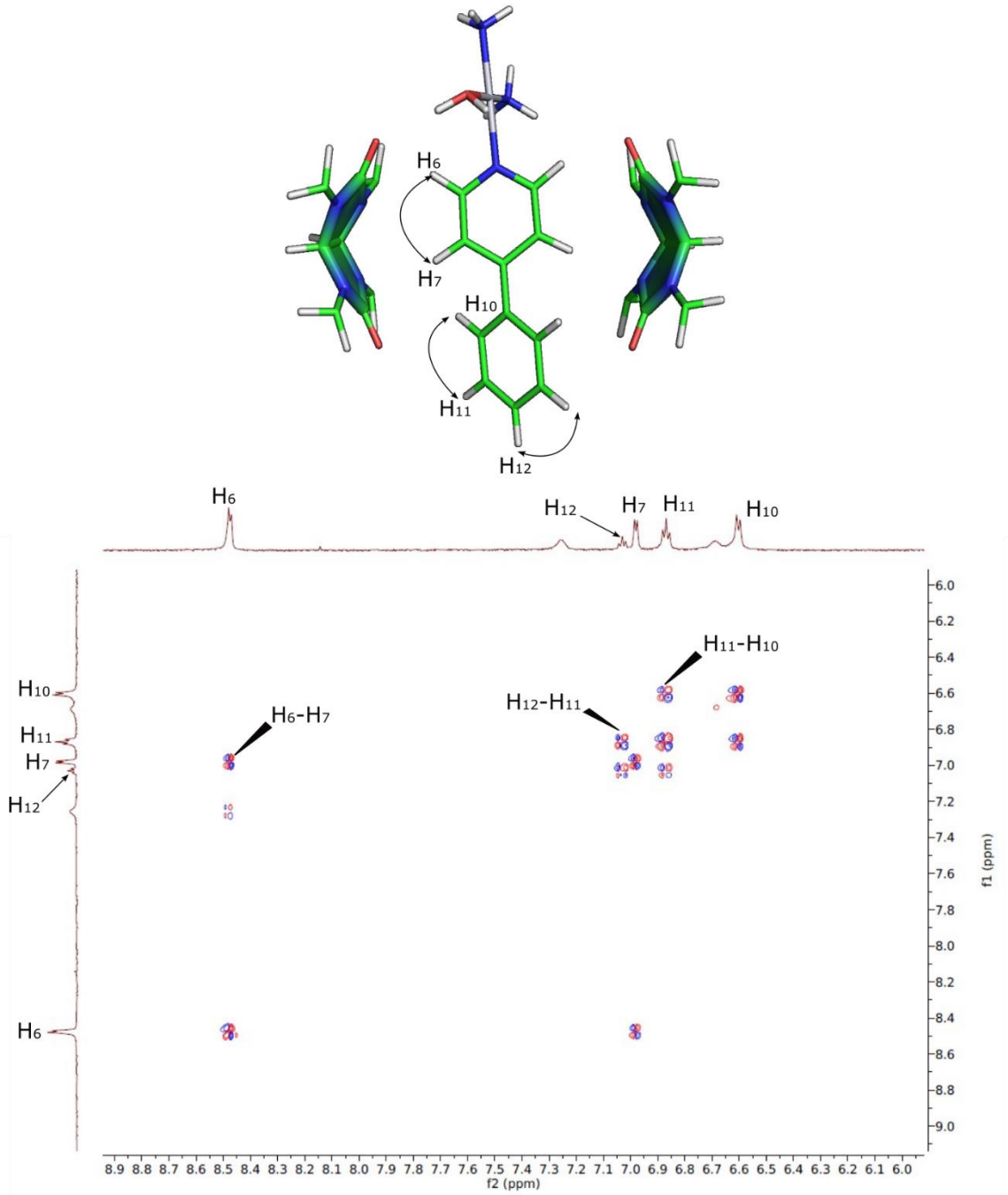

Figure S21. ^{1}H-^{1}H DQF-COSY spectrum of **3@CB7/3_aq@CB7** measured in water at 298 K.

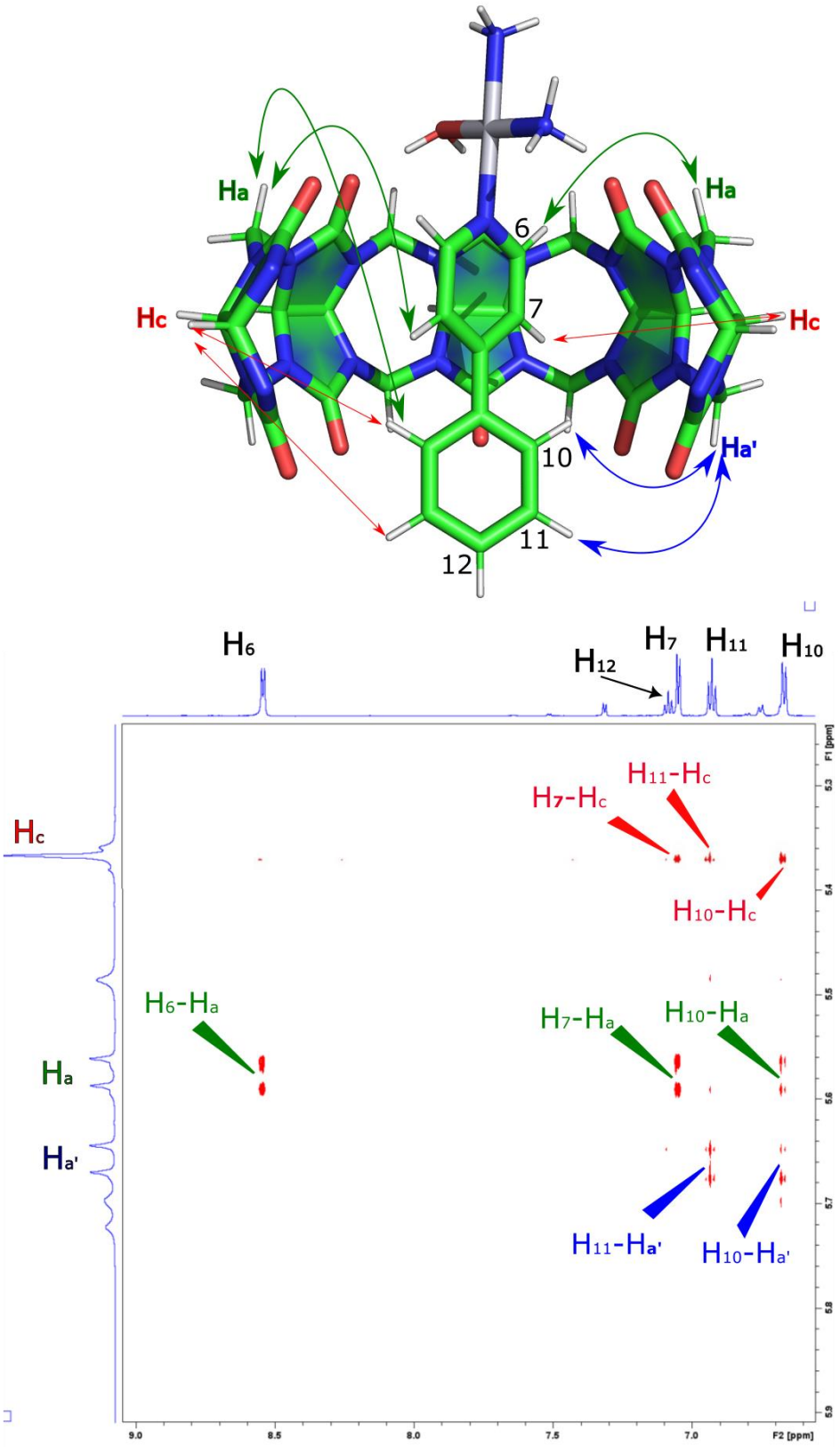

Figure S22. ^{1}H-^{1}H ROESY spectrum of **3_aq@CB7** measured in water at 298 K.

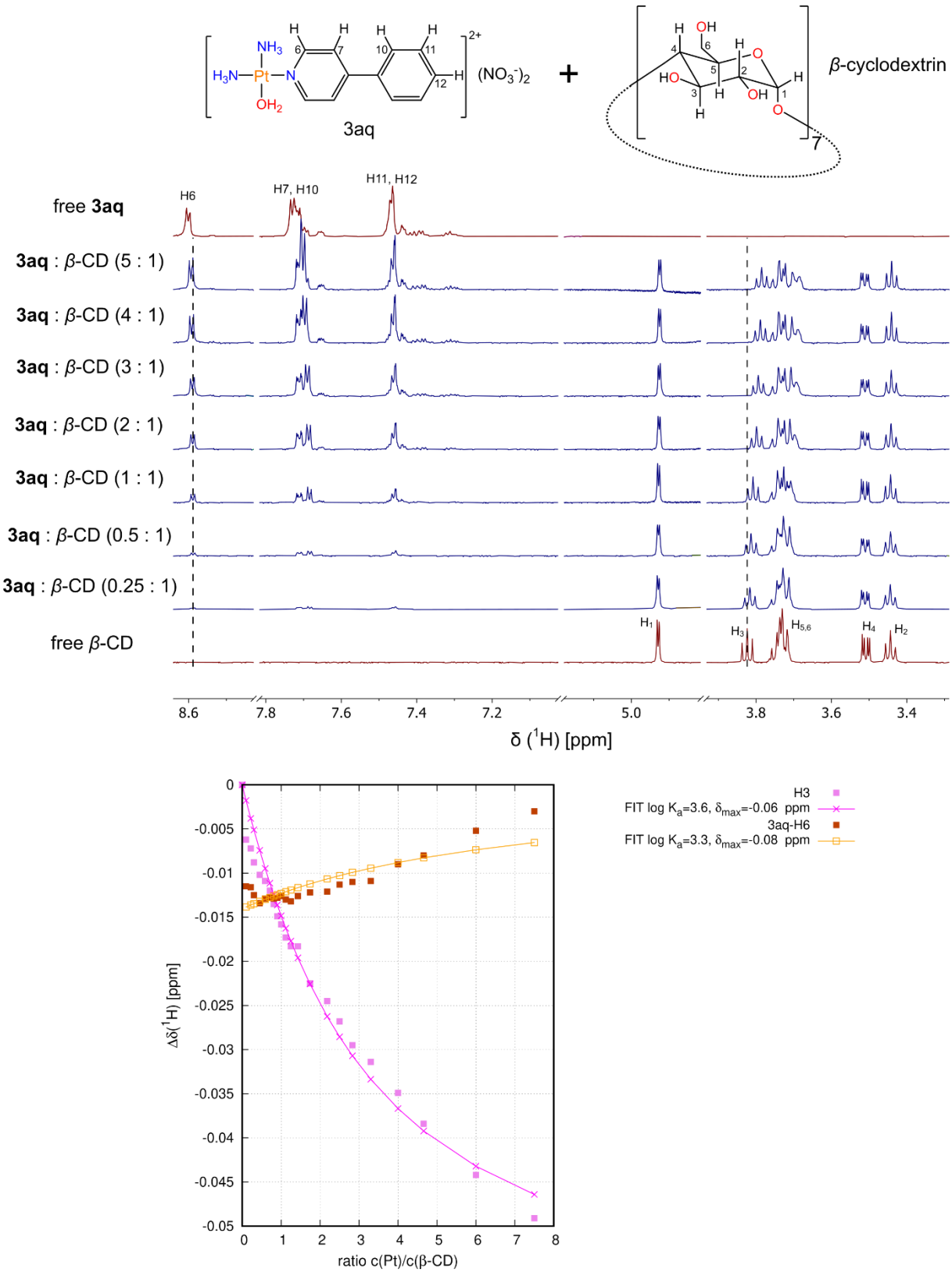

Figure S23a. Record of ^{1}H NMR titration of compound **3_aq** into *β*-CD (c = 0.1 mM) measured in D_2O at 298 K.

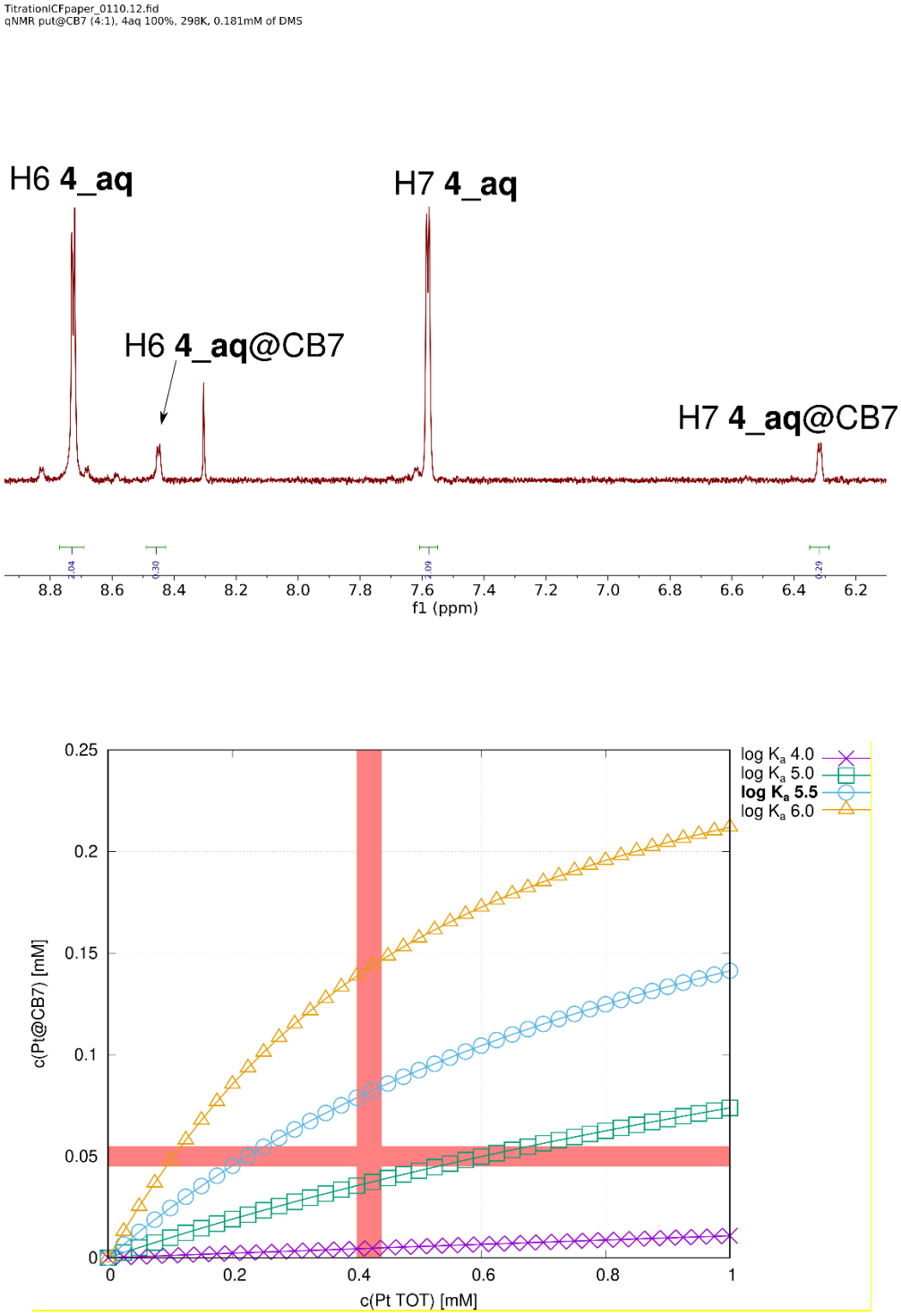

Figure S23b. ^{1}H NMR of compound **4_aq** (0.40 mM) mixed with CB7 (0.30 mM) in the presence of putrescine dihydrochloride as a competitor (1.12 mM, logK_a~5.5) measured in D_2O at 298 K. Plot in the bottom shows simulated dependence of the concentration of **4_aq** bound in CB7 as a function of total **4_aq** concentration and various binding constants.

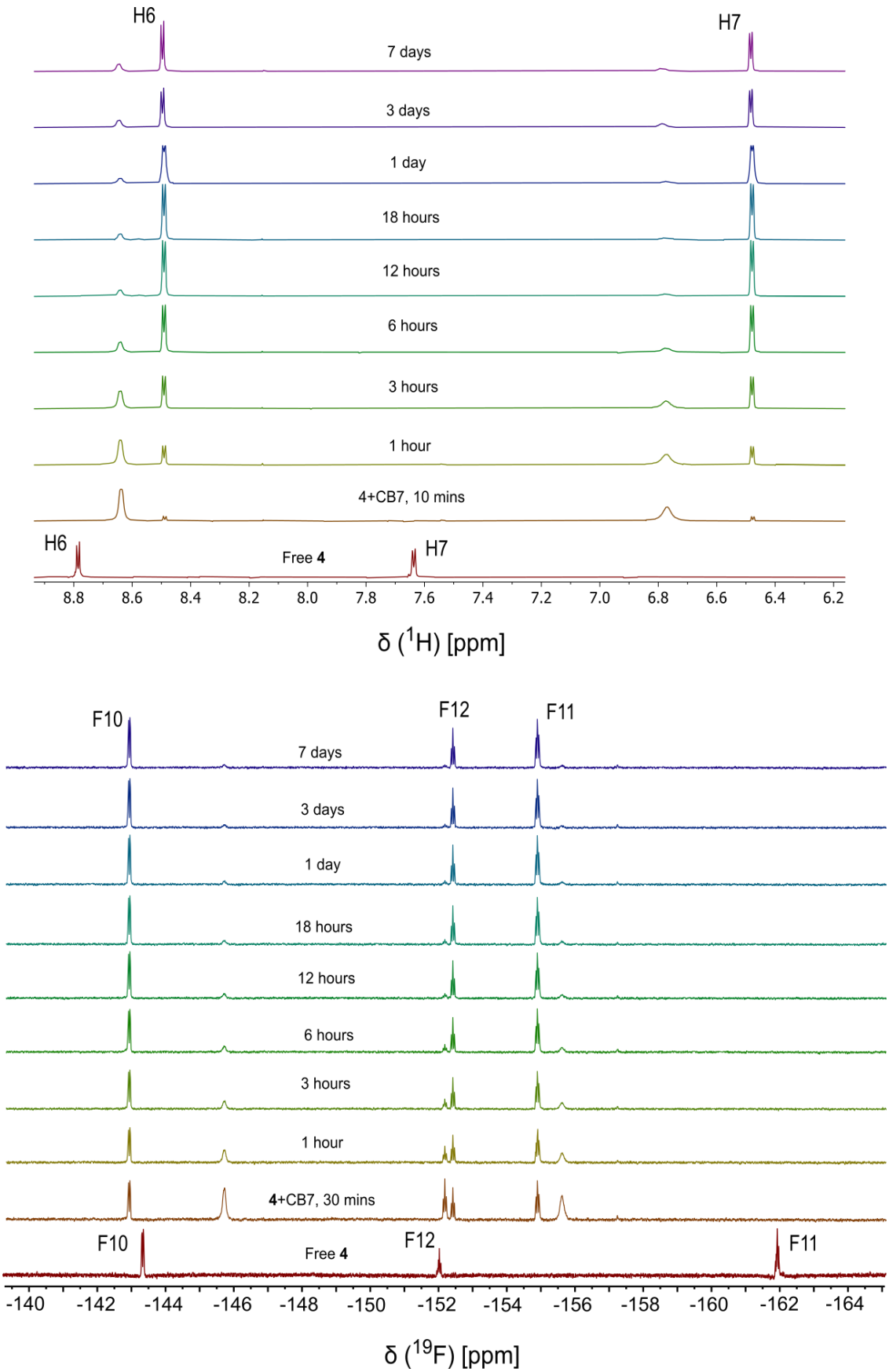

Figure S24a. ^{1}H NMR (top) and ^{19}F NMR (bottom) spectra of the guest part of **4@CB7** measured at several different times of aquation in water at 298 K.

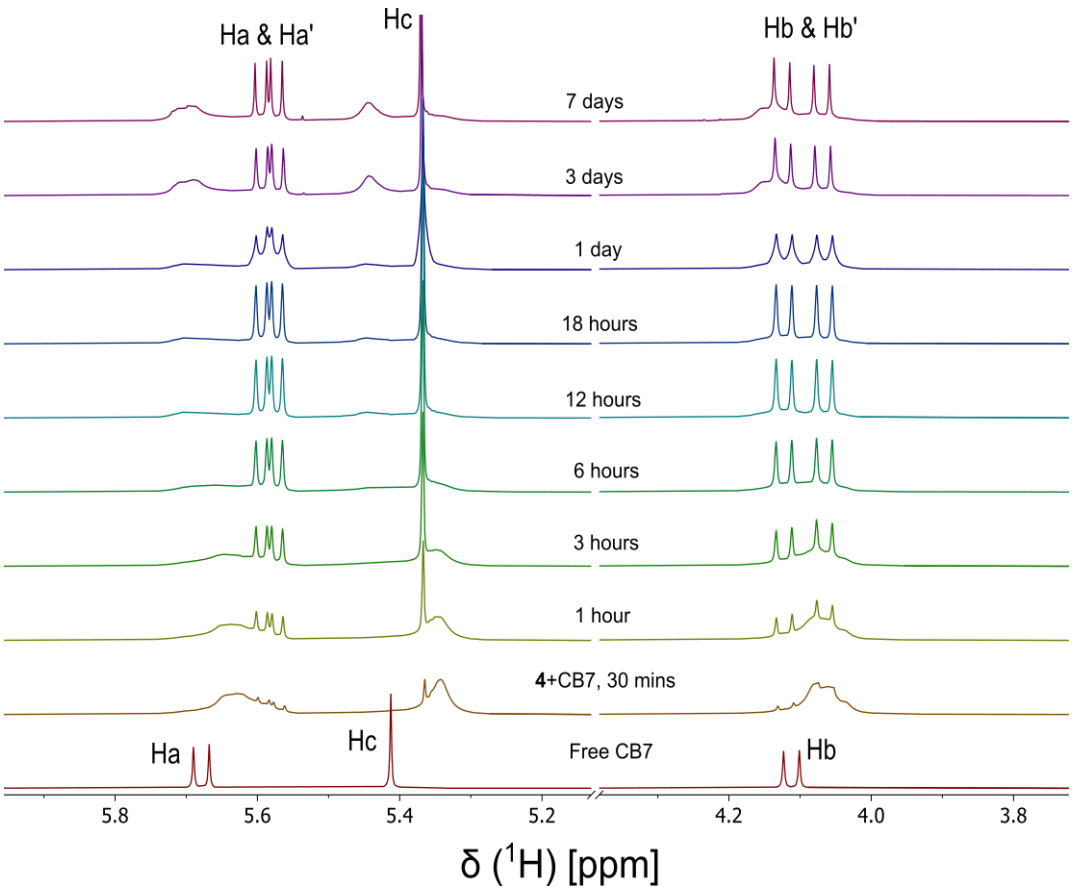

Figure S24b. ^{1}H NMR spectra of the host part of **4@CB7** measured at several different times of aquation in water at 298 K.

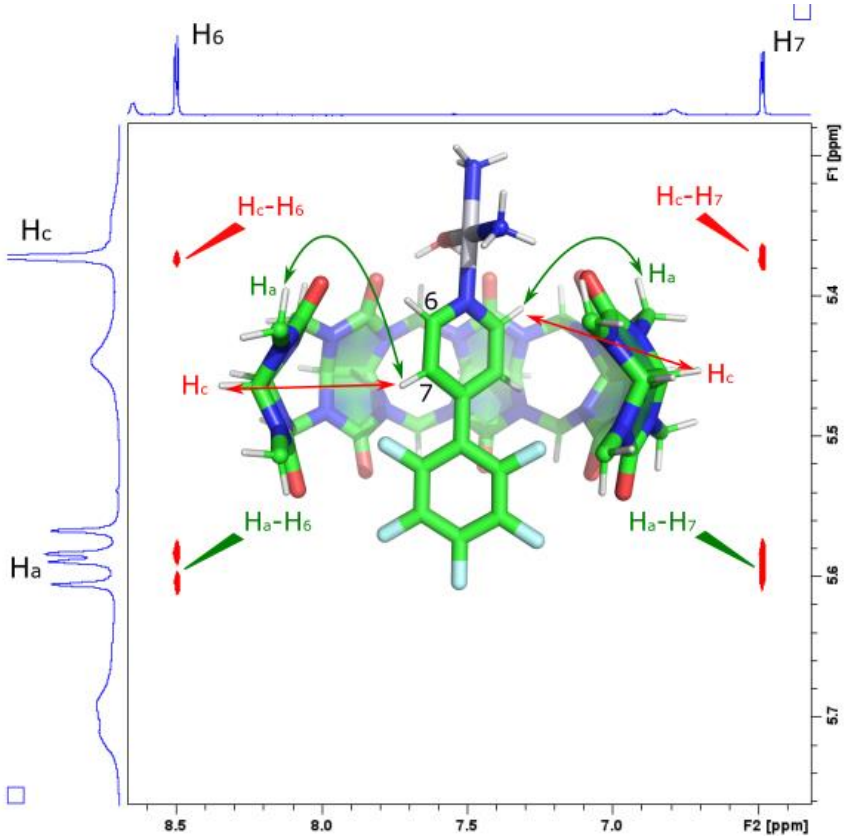

Figure S25. ^{1}H-^{1}H ROESY spectrum of **4@CB7** (~ **4_aq@CB7**).

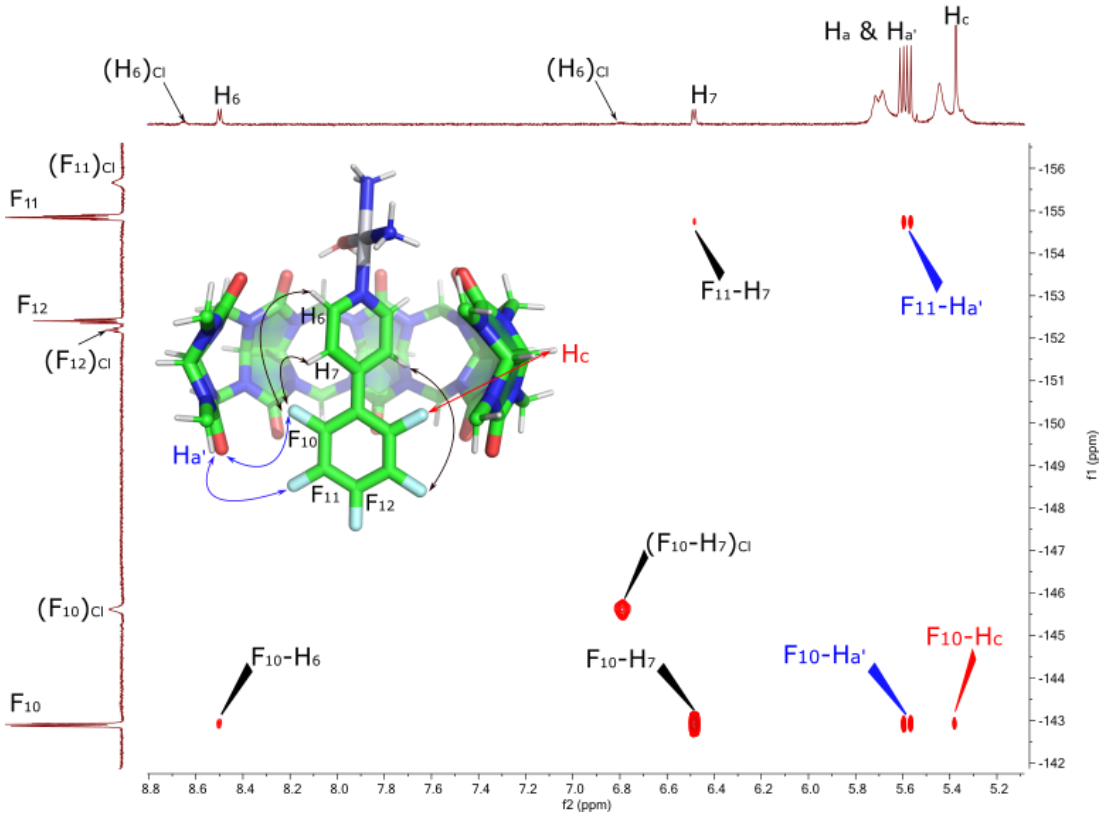

Figure S26. ^{1}H-^{19}F NOESY (HOE) spectrum of **4@CB7/4_aq@CB7**.

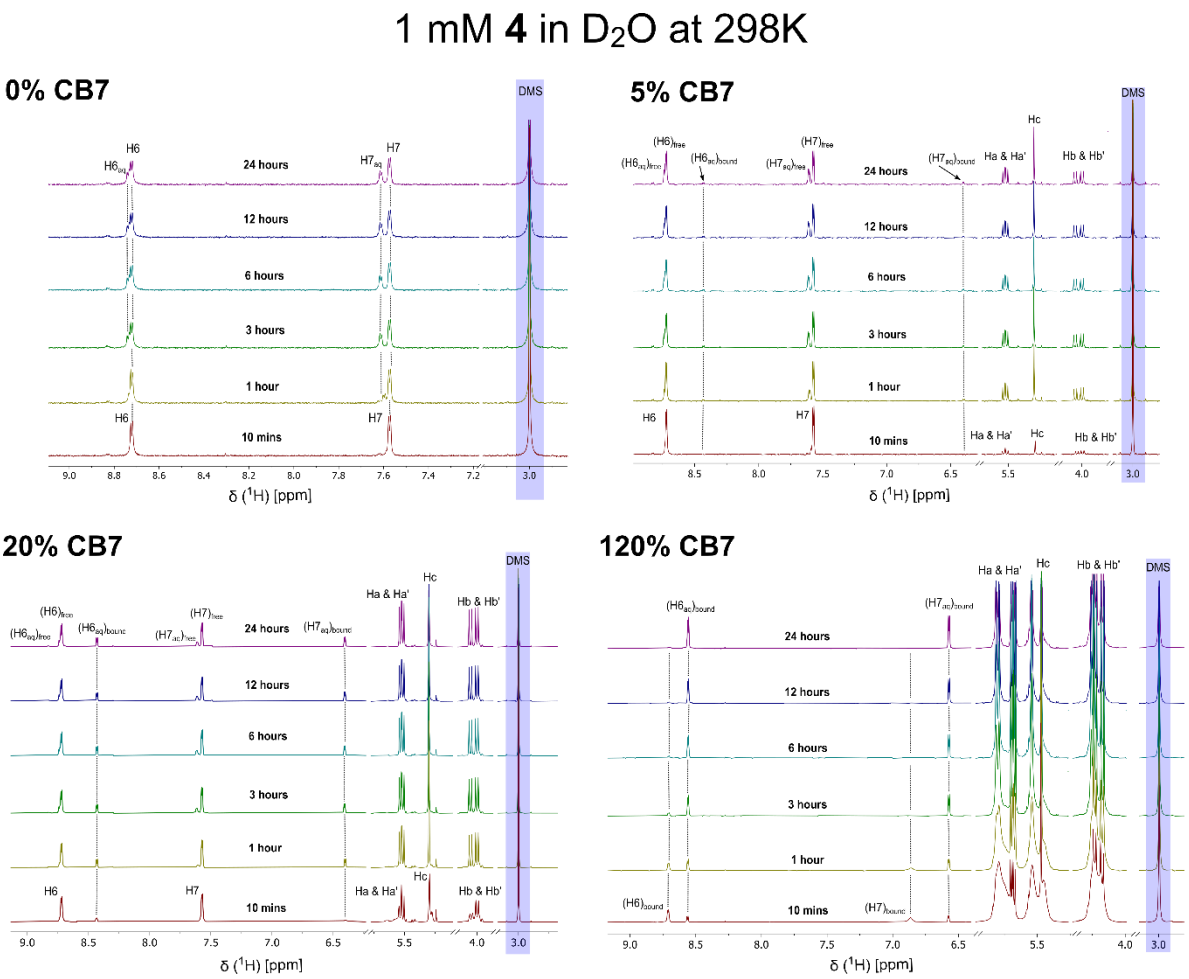

Figure S27. ^{1}H NMR spectra of **4_aq** (1 mM solution) with addition of CB7 (0%, 5%, 20%, and 120%) measured at several different time of sample aquation in D_2O at 298 K.

S4. SOLUBILITY MEASUREMENT USING ICP-MS

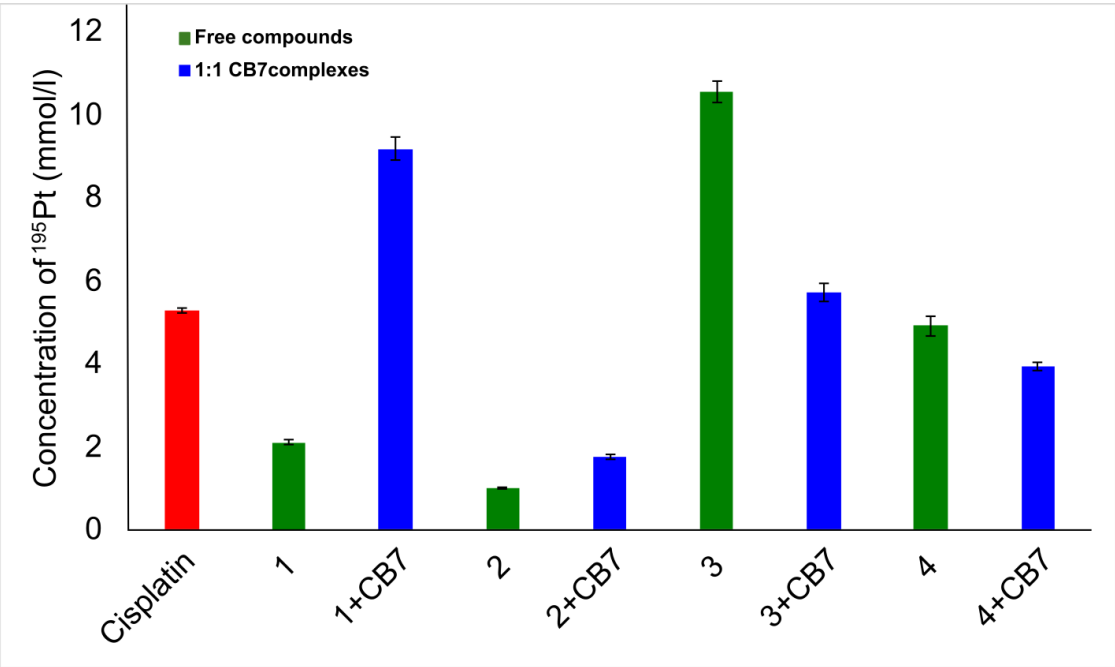

Figure S28. Solubility (concentration in mM) of cisplatin and compounds **1**-**4** and their HG complexes with CB7 in water at 295 K as determined by ICP-MS.

S5. MOLECULAR MODELLING

S5.1. MM parametrization of host

The initial structures for the host molecules were generated in Avogadro and minimized with the UFF force field.[4] Structures were then pre-optimized in Orca using the B3LYP[5] functional and def2-TZVPP basis set in implicit water solvent model. Parametrization of the metal center was performed by the MCPB.py module in Amber 22 package. We employed a bonded model approach, bond and angle force constants were calculated with the Seminario method, force constants for the dihedral angles were initially neglected (as per default by MCPB.py). Geometry optimization, frequency and esp calculations were all performed in Gaussian 16.C1[6] package with same the setup that was used in the Orca pre-optimization. Ligands were parametrized using the gaff2 force field.

S5.2. MM parametrization of guest

Initial structure was obtained from the work of Kulhánek et al.[7] It was then re-optimized in Orca and described by the gaff2 force field. Atomic charges were obtained by the standard RESP[8] procedure. Esp calculation was performed in Gaussian 16.C1. All DFT calculations were performed with the same level of theory as the host structures.

S5.3. Unbiased MD simulation - calculation setup

After parametrization, complexes were manually assembled in PyMol[9] and then processed with the *tleap* program from the Amber 22 package. The complexes were solvated with OPC[10] type water with 12 Å thick shell in the truncated octahedral box. The net charge was neutralized with Cl^- anions.

Periodic boundary conditions were used. Particle-mesh Ewald method (PMEM)[11] was used to handle the long-range interactions. The cutoff used both for PMEM and Lennard-Jones interactions was set to 8 Å. Time step used for integration was 2 fs, SHAKE[12] algorithm was used for constraining the bonds that involve hydrogen atoms.

Before the performance of the MD run, the whole system was gradually equilibrated in ten steps. First, only the solvent atoms were optimized, while the complex was restrained. The system was then heated to 300 K for the duration of 100 ps at the constant volume using the Langevin thermostat with the collision frequency of 5 ps^{-1}, while the complex was restrained. System was then gradually equilibrated at constant pressure of 1 bar (Monte Carlo barostat) with the same thermostat; collision frequency was adjusted to 2 ps^{-1}. Restrain on the system was getting smaller every step. Final equilibration was run for 300 ps with the same setup described earlier with no restraints imposed on the system.

MD simulation was then performed on the equilibrated system. Simulation was held at the constant temperature 300 K with Langevin thermostat, employing the ’middle’ thermostat scheme based on the leapfrog algorithm. Reference pressure was set to 1 bar, pressure was

regulated by isotropic position scaling with Monte Carlo barostat. Production dynamics were calculated by a GPU[13] accelerated version of the *pmemd* package in Amber. Total simulated time was 2 μs.

S5.4. Unbiased MD simulation - analysis

All of the trajectory analyses were performed with the help of the *cpptraj* program from the Amber package. To analyze the stability of the complexes, oriented distance was calculated for each snapshot.

S5.5. Adaptive Biasing Force simulations - calculation setup

The Adaptive Biasing Force[14,15] (ABF) method was employed to calculate the free energy profiles of the complexes. All ABF calculations were done using the PMFLib[16] package connected with the pmemd program from the Amber package. To improve the sampling along the chosen collective variables, Multiple Walker Approach (MWA) was employed, which utilizes a server/client architecture with fully asynchronous communication pattern. More detailed description of the implementation of the method can be found at the work of Kulhánek *et al.* [17]

MD setup for the ABF simulation was the same as described earlier in the MD section. For each ABF simulation, ten clients were employed. Exchange of the mean force between the clients and server was performed every 40 ps. Each client started from the different configuration of the system. These were taken from the unbiased MD run, separated by 10 ns each. Integration of the mean forces was performed using the RFD algorithm.

S5.6. Collective Variables

To explore the dissociation of the complexes, oriented distance (ODIS, *D*) was chosen as a sampling collective variable (CV). ODIS is defined as a distance between the plane and point, where the point was defined as a center of mass of ring C and N atoms of phenylpyridine moiety (group A) and plane was defined by the middle plane carbon atoms of the cucurbituril molecule

(group B). ODIS was sampled in interval that ranges from -2 to 15 Å with the bin size of 0.1 Å. Outside this interval, harmonic potential was applied with force constant 4 kcal mol^{-1} $Å^{-2}$.

To further improve the sampling along ODIS, two helper CVs were employed. ORAD, defined as the radial distance of the point (defined by group A) from z-axis of reoriented coordinate system along principal moments of the tensor inertia I (defined by group B), was employed to prevent the guest escaping the imaginative cylinder defined by the host.
When the value of ORAD exceeded 2.5 Å force constant of magnitude 4 kcal mol^{-1} $Å^{-2}$ was applied. Finally, PVANG, the angle between the normal vector of the plane (defined by group B) and the vector pointing from the point B (defined by the C12 phenylpyridine atom) to the point C (defined by the Pt atom), was employed to prevent the guest from rotating out of axial orientation. It was constrained to the interval (-5; 5)°. Outside of it, force constant of magnitude 4 kcal mol^{-1} deg^{-2}) was applied.

S5.7. Effect of the planarity

Since MCPB.py neglects the dihedral torsions, we wanted to explore the effects of it on the overall ODIS of the complex **3_aq**. For this, we chose the improper torsion defined by the atom sequence C6-Pt-N5-C7, thus impacting the deviation of the Pt from the plane of the aromatic ring. We prepared seven different systems in the *tleap*, each differing in the value of the force constant of the improper torsion. For each system, production run was performed with the same setup as described before and subsequently the ODIS and NICS were calculated.

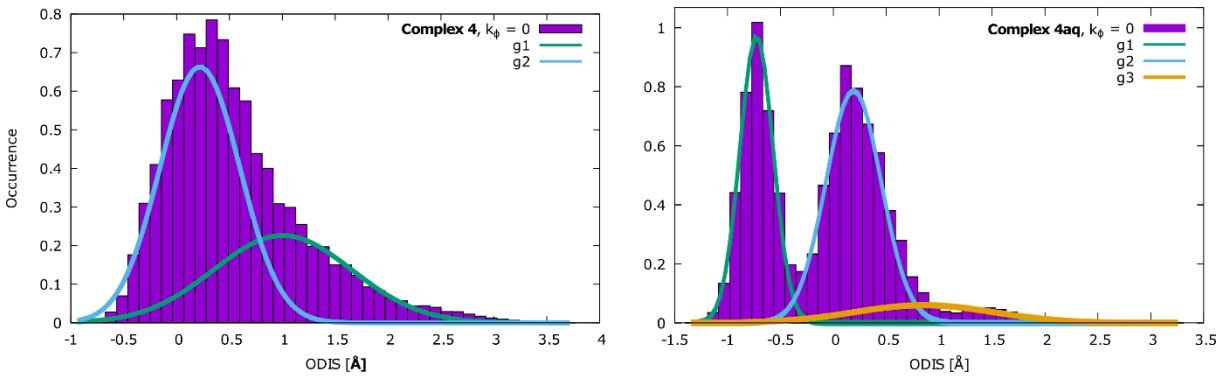

Figure S29. Distribution of oriented distance (ODIS) of compound **4** (left) and **4_aq** (right) with respect to middle plane of CB7. Note additional position around -0.75Å representing more compact encapsulation of ligand in case of aquated form **4_aq**.

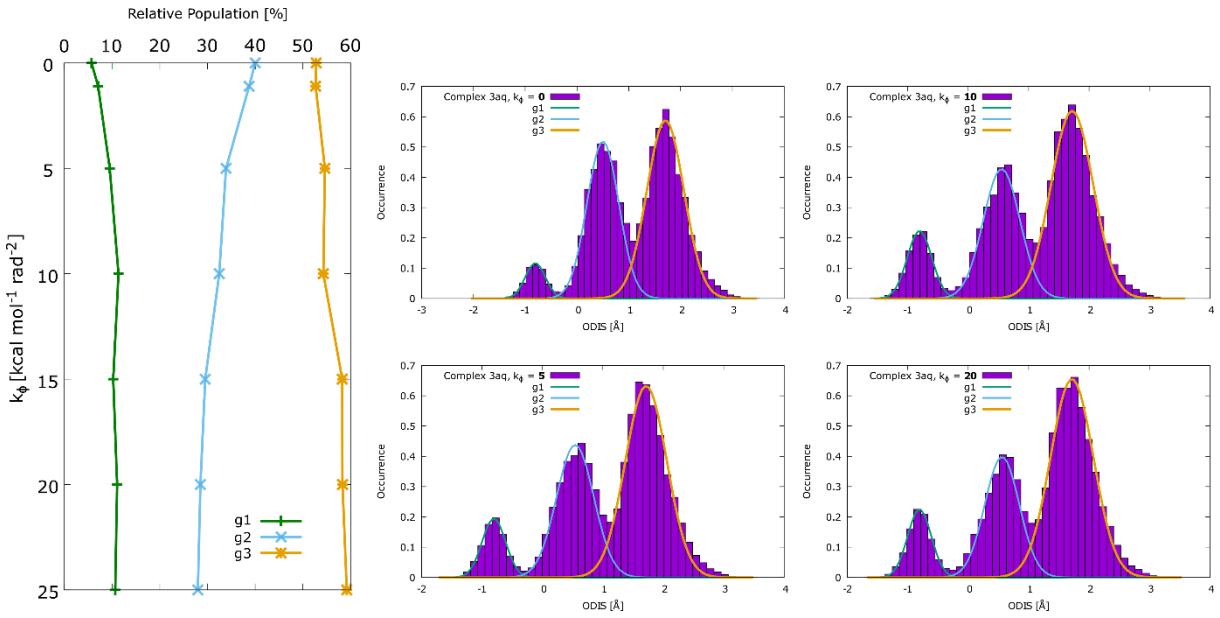

Figure S30. Effect of scaled force constant k_Φ intended to keep planarity of the Pt center relative to aromatic ring in the MD simulation of **3_aq@CB7** (for details, see section Methods). The ODIS histograms (shown for k_Φ = 0, 5, 10, 20 kcal mol^{-1} Φ^{-2}) are evaluated by means of three gaussian curves (g1, g2, g3) fitted the distribution of oriented distance as obtained from 2 μs trajectories.

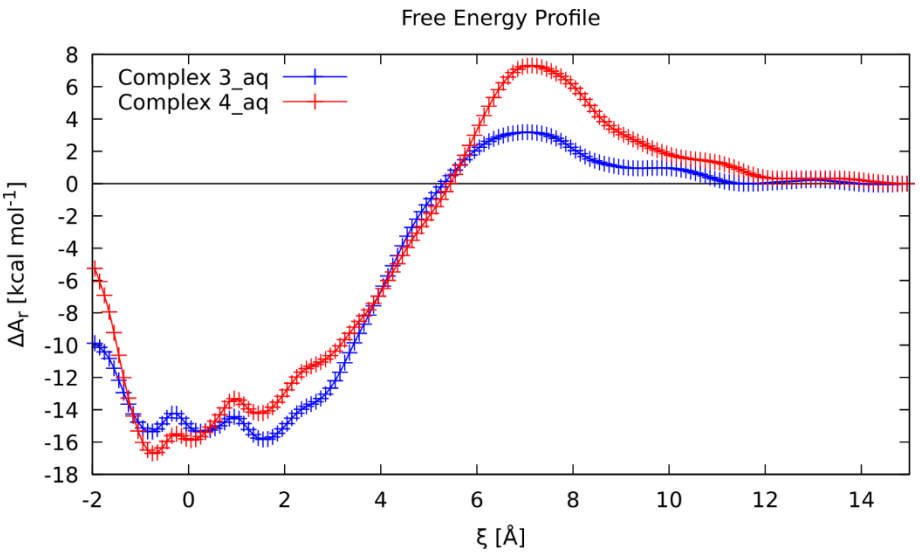

Figure S31. Free energy profile of dissociation of **3_aq@CB7** and **4_aq@CB7** calculated using ABF approach (for computational setup, see section Methods). There are two key differences between binding processes of **3_aq** vs **4_aq**: Position of global minima is shifted ~2.5 Å towards bound form for **4_aq@CB7**. We also detected two times higher barrier (8 vs 4 kcal mol^{-1}) of encapsulation for **4_aq@CB7**. Free energy profiles also indicate narrower distribution of bound state of **4_aq**.

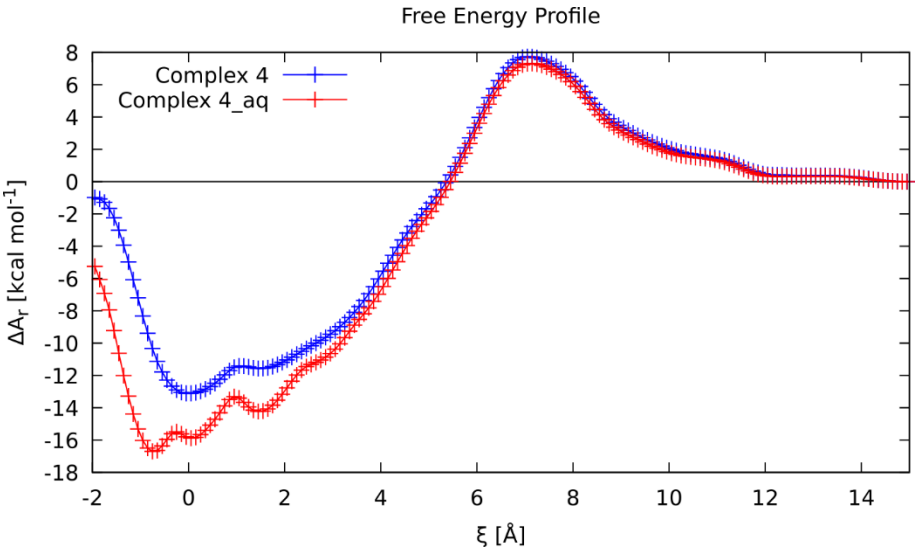

Figure S32. Free energy profile of dissociation of **4@CB7** and **4_aq@CB7**. The effect of aquation and doubled charge of guest results in a shift of global minimum and its stabilization by 4 kcal mol^{-1}. On the contrary the energy barrier of encapsulation remains unaffected.

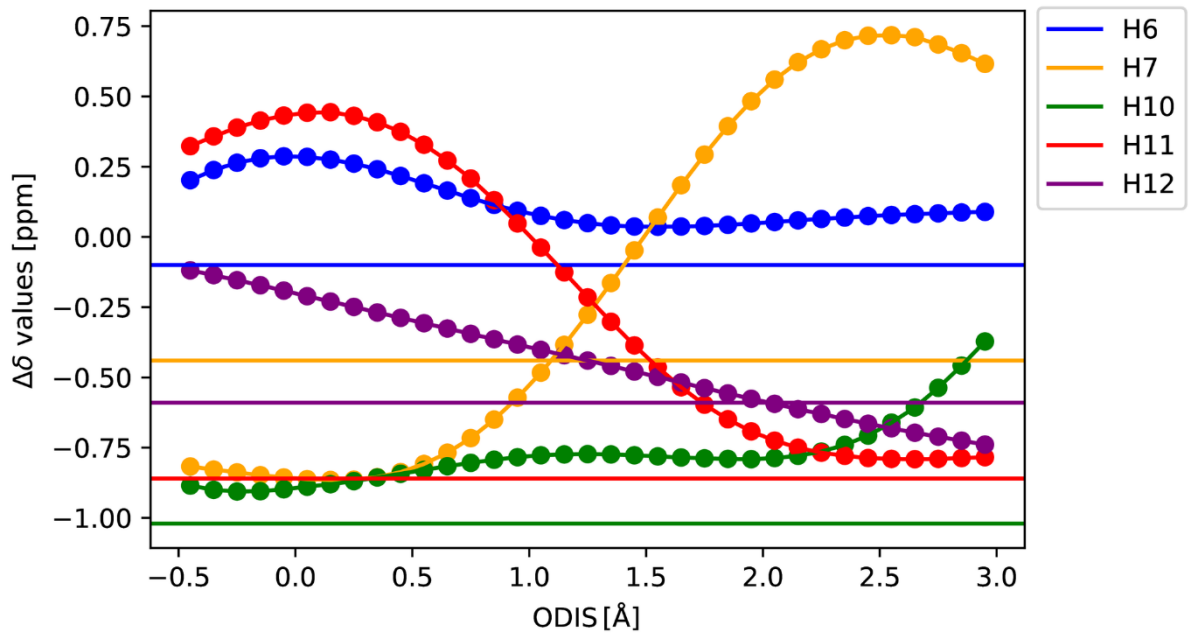

Figure S33. Dependence of the calculated $\Delta\delta$ values on the Oriented Distance of **3@CB7**. Each curve represents one NMR active atom. Each horizontal line represents measured experimental value for the corresponding atom. The positive contributions to the curves arise from the region of the carbonyl rim, negative contributions represent a situation when the atom is inside the cavity. Bolztmann weighted averages of these curves are represented in the main text along side experimental values in Figure 6.

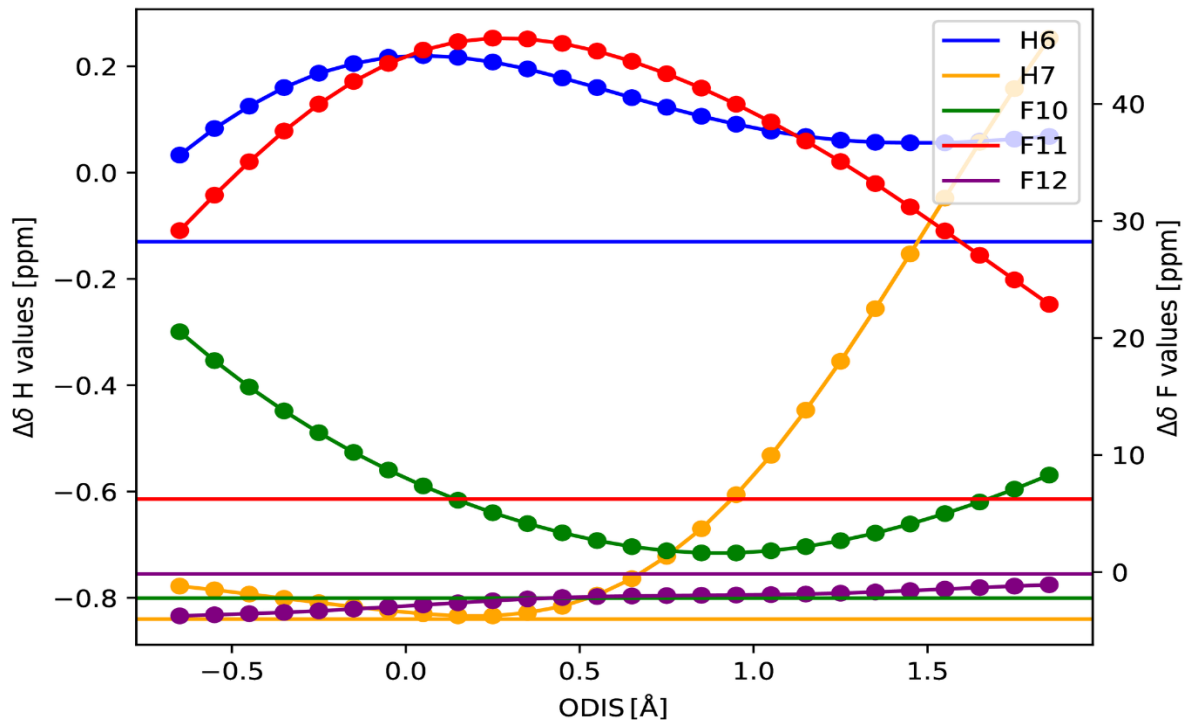

Figure S34. Dependence of the calculated $\Delta\delta$ values on the Oriented Distance of **4@CB7**. Separate scaling of *y*-axis is introduced for the hydrogen and fluorine atoms.

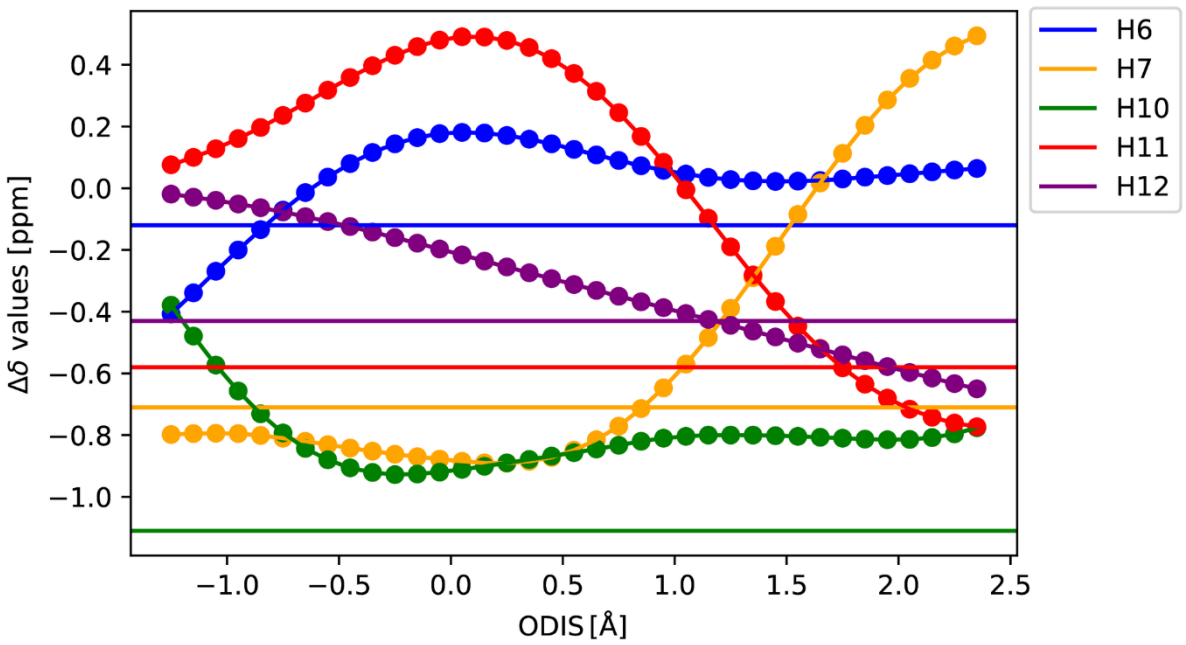

Figure S35. Dependence of the calculated Δδ values on the Oriented Distance of **3_aq@CB7**.

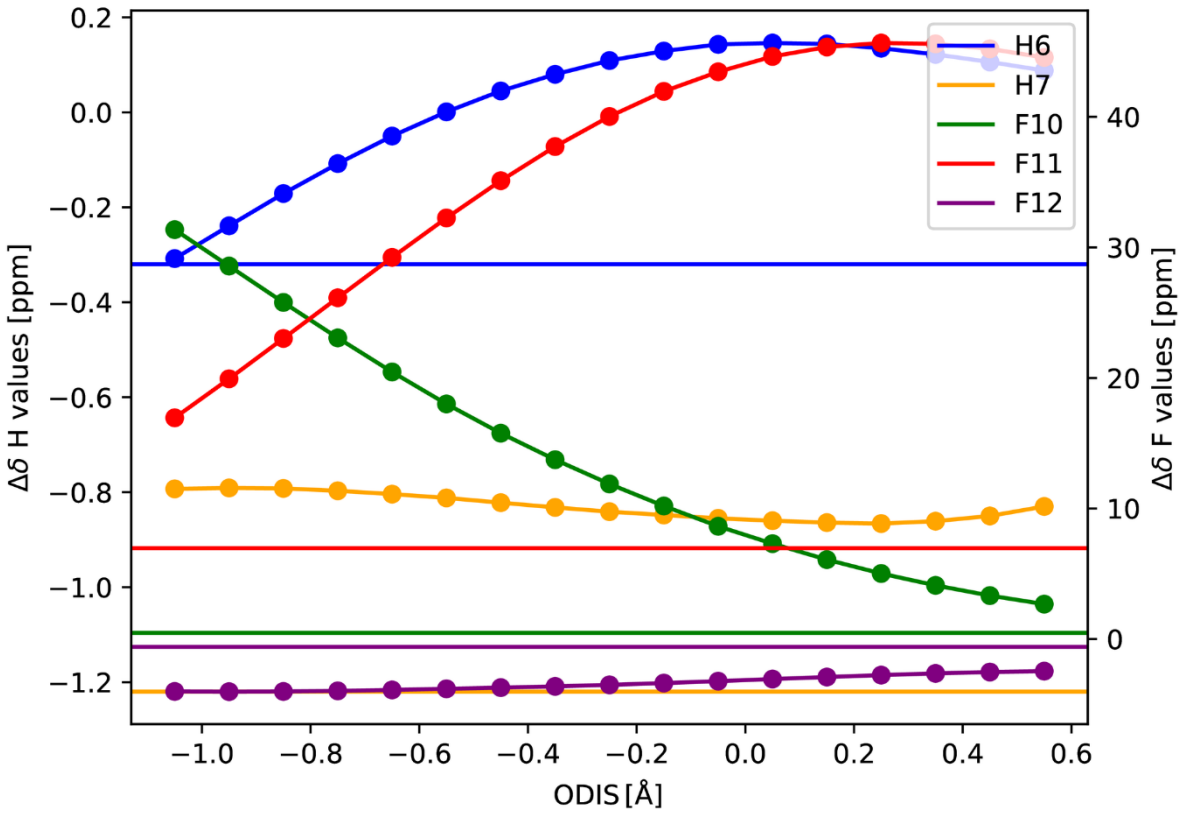

Figure S36. Dependence of the calculated Δδ values on the Oriented Distance of **4_aq@CB7**. Separate scaling of *y*-axis is introduced for the hydrogen and fluorine atoms.

Table S5. Theoretical Δδ values and the experimental NMR shifts for **3_aq@CB7**.

Atom	$\Delta\delta$ [ppm]			
	NICS-MD[a]	NICS-QM[b]	Rigid Scan[c]	Experiment
H6	-0.10	-0.29	0.04	-0.12
H7	-0.78	-0.78	-0.49	-0.71
H10	-0.77	-0.80	-0.82	-1.11
H11	-0.75	-0.58	-0.01	-0.58
H12	-0.40	-0.27	-0.33	-0.43

[a]*NICS-MD* refers to the average of the distributions that resulted from the projecting of the calculated NICS grid onto the geometries from the MD simulation. [b]*NICS-QM test* referes to the values calculated by projecting the NICS grid onto the structures that were used for the explicit QM calculation (Rigid Scan). [c]*Rigid Scan* was already showed in the main text. While the average values from the original MD NICS calculation are in better numerical agreement with the experiment, they fail to reproduce the clear trends in $\Delta\delta$ values which are observed in the experiment. This is generally case for all studied systems. However, altough the values from the rigid scan replicate the experimental trends to some extend, there are bigger numerical discrepancies, the most obvious example being atom H11. The sources of the discrepancies can be numerous, including the used method (functional, basis set, etc.), model (e.g. missing solvation layer around carbonyl portal, different pH used in the experiment) and the energy profile that was used to calculate the populations of the which were then used to weight the final $\Delta\delta$ values. Finally, the numbers from the test NICS calculation show that even when various structural motifs such as tilting of the host are omitted from the model, it does not really matter.

REFERENCES

(1) Bonakdarzadeh, P.; Topić, F.; Kalenius, E.; Bhowmik, S.; Sato, S.; Groessl, M.; Knochenmuss, R.; Rissanen, K. DOSY NMR, X-Ray Structural and Ion-Mobility Mass Spectrometric Studies on Electron-Deficient and Electron-Rich M6L4 Coordination Cages. *Inorg. Chem.* **2015**, *54* (12), 6055–6061. https://doi.org/10.1021/acs.inorgchem.5b01082.

(2) Ma Tiantian; Nie Qiqi; Feng Zhen; Li Hongyan; Sha Xunshan; Sun Zhanyi; Wang Yalong. Shanxi Laite Optoelectric Materials Co., Ltd. CN110183333, 2019.

(3) Thapa, S.; Kafle, A.; Gurung, S. K.; Montoya, A.; Riedel, P.; Giri, R. Ligand-Free Copper-Catalyzed Negishi Coupling of Alkyl-, Aryl-, and Alkynylzinc Reagents with Heteroaryl Iodides. *Angew. Chem. Int. Ed.* **2015**, *54* (28), 8236–8240. https://doi.org/10.1002/anie.201502379.

(4) Rappe, A. K.; Casewit, C. J.; Colwell, K. S.; Goddard, W. A. I.; Skiff, W. M. UFF, a Full Periodic Table Force Field for Molecular Mechanics and Molecular Dynamics Simulations. *J. Am. Chem. Soc.* **1992**, *114* (25), 10024–10035. https://doi.org/10.1021/ja00051a040.

(5) Becke, A. D. Density-functional Thermochemistry. III. The Role of Exact Exchange. *J. Chem. Phys.* **1993**, *98* (7), 5648–5652. https://doi.org/10.1063/1.464913.

(6) M. J. Frisch, G. W. Trucks, H. B. Schlegel, G. E. Scuseria, M. A. Robb, J. R. Cheeseman, G. Scalmani, V. Barone, G. A. Petersson, H. Nakatsuji, X. Li, M. Caricato, A. V. Marenich, J. Bloino, B. G. Janesko, R. Gomperts, B. Mennucci, H. P. Hratchian, J. V. Ortiz, A. F. Izmaylov, J. L. Sonnenberg, D. Williams-Young, F. Ding, F. Lipparini, F. Egidi, J. Goings, B. Peng, A. Petrone, T. Henderson, D. Ranasinghe, V. G. Zakrzewski, J. Gao, N. Rega, G. Zheng, W. Liang, M. Hada, M. Ehara, K. Toyota, R. Fukuda, J. Hasegawa, M. Ishida, T. Nakajima, Y. Honda, O. Kitao, H. Nakai, T. Vreven, K. Throssell, J. A. Montgomery, Jr., J. E. Peralta, F. Ogliaro, M. J. Bearpark, J. J. Heyd, E. N. Brothers, K. N. Kudin, V. N. Staroverov, T. A. Keith, R. Kobayashi, J. Normand, K. Raghavachari, A. P. Rendell, J. C. Burant, S. S. Iyengar, J. Tomasi, M. Cossi, J. M. Millam, M. Klene, C. Adamo, R. Cammi, J. W. Ochterski, R. L. Martin, K. Morokuma, O. Farkas, J. B. Foresman, and D. J. Fox. Gaussian 16.

(7) Branná, P.; Černochová, J.; Rouchal, M.; Kulhánek, P.; Babinský, M.; Marek, R.; Nečas, M.; Kuřitka, I.; Vícha, R. Cooperative Binding of Cucurbit[n]Urils and β-Cyclodextrin to Heteroditopic Imidazolium-Based Guests. *J. Org. Chem.* **2016**, *81* (20), 9595–9604. https://doi.org/10.1021/acs.joc.6b01564.

(8) Cieplak, P.; Cornell, W. D.; Bayly, C.; Kollman, P. A. Application of the multimolecule and multiconformational RESP methodology to biopolymers: Charge derivation for DNA, RNA, and proteins. *J. Comp. Chem.* **1995**, *16* (11), 1357–1377. https://doi.org/10.1002/jcc.540161106.

(9) The PyMOL Molecular Graphics System, Version 1.2r3pre, Schrödinger, LLC.

(10) Izadi, S.; Anandakrishnan, R.; Onufriev, A. V. Building Water Models: A Different Approach. *J. Phys. Chem. Lett.* **2014**, *5* (21), 3863–3871. https://doi.org/10.1021/jz501780a.

(11) Darden, T.; York, D.; Pedersen, L. Particle Mesh Ewald: An N·log(N) Method for Ewald Sums in Large Systems. *J. Chem. Phys.* **1993**, *98* (12), 10089–10092. https://doi.org/10.1063/1.464397.

(12) Ryckaert, J.-P.; Ciccotti, G.; Berendsen, H. J. C. Numerical Integration of the Cartesian Equations of Motion of a System with Constraints: Molecular Dynamics of n-Alkanes. *J. Comp. Phys.* **1977**, *23* (3), 327–341. https://doi.org/10.1016/0021-9991(77)90098-5.

(13) Salomon-Ferrer, R.; Götz, A. W.; Poole, D.; Le Grand, S.; Walker, R. C. Routine Microsecond Molecular Dynamics Simulations with AMBER on GPUs. 2. Explicit

Solvent Particle Mesh Ewald. *J. Chem. Theory Comput.* **2013**, *9* (9), 3878–3888. https://doi.org/10.1021/ct400314y.
(14) Darve, E.; Rodríguez-Gómez, D.; Pohorille, A. Adaptive Biasing Force Method for Scalar and Vector Free Energy Calculations. *J. Chem. Phys.* **2008**, *128* (14), 144120. https://doi.org/10.1063/1.2829861.
(15) Comer, J.; Gumbart, J. C.; Hénin, J.; Lelièvre, T.; Pohorille, A.; Chipot, C. The Adaptive Biasing Force Method: Everything You Always Wanted To Know but Were Afraid To Ask. *J. Phys. Chem. B* **2015**, *119* (3), 1129–1151. https://doi.org/10.1021/jp506633n.
(16) *PMFLib*. https://pmflib.ncbr.muni.cz/ (accessed 2023-12-22).
(17) Bouchal, T.; Durník, I.; Illík, V.; Réblová, K.; Kulhánek, P. Importance of Base-Pair Opening for Mismatch Recognition. *Nucleic Acids Res.* **2020**, *48* (20), 11322–11334. https://doi.org/10.1093/nar/gkaa896.